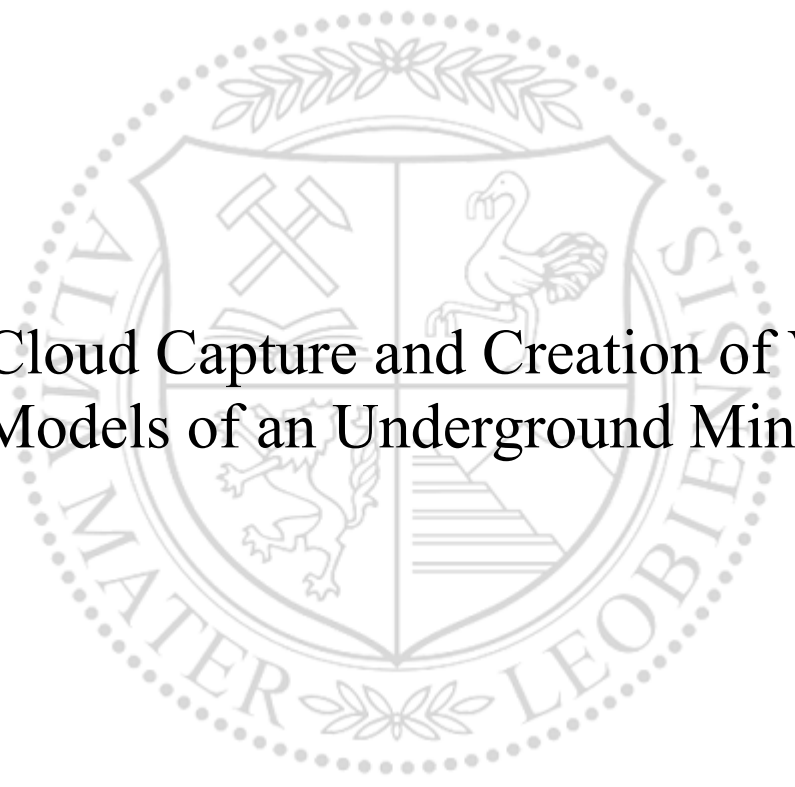


Chair of Mining Engineering and Mineral Economics

Master's Thesis



Point Cloud Capture and Creation of Virtual  
Reality Models of an Underground Mining Drift

Diogo Sebastiao Lopes de Pinho

June 2024



**AFFIDAVIT**

I declare on oath that I wrote this thesis independently, did not use any sources and aids other than those specified, have fully and truthfully reported the use of generative methods and models of artificial intelligence, and did not otherwise use any other unauthorized aids.

I declare that I have read, understood and complied with the "Good Scientific Practice" of the Montanuniversität Leoben.

Furthermore, I declare that the electronic and printed versions of the submitted thesis are identical in form and content.

Date 16.06.2024

*Diogo Sebastiao Lopes de Pinho*

Signature Author

Diogo Sebastiao Lopes de Pinho

## Abstract

This study focuses on assessing the iPhone 13 pro and 5<sup>th</sup> iPad Pro laser scanning abilities to create 3D models of mine drifts with sufficient detail to retrieve geological and geotechnical features and elaborate immersive Virtual Reality models.

A drift of the Neves-Corvo mine was scanned using the iPhone 12 Pro, the 5<sup>th</sup> generation iPad Pro, the Faro Focus S70 laser scanner and the Leica MS60 multistation. The apple devices scans were collected by mobile laser scanning while the other by terrestrial laser scanning. These scans were subject to a quantitative analysis, regarding the resolution, time-effectiveness, user-friendliness and density. A qualitative analysis of the Apple's and Faro's scans was conducted regarding their capability of retrieving color and imagery, and thus applicability to assess geological and geotechnical features. Furthermore, the possibility to create Virtual Reality models from the apple and Faro scans was evaluated. Lastly, one of the scans retrieved with the iPhone 13 Pro was used to successfully perform rock mass classification through the Q-System. The apple devices revealed adequate resolution and point density to correctly represent the mine drift, despite inferior values than the scans captured with the Faro Focus laser scanner. On the other hand, the iPhone and iPad were more proficient in retrieving the color of the rock mass and presented a quicker and more user-friendly option to create VR models, due to the higher compatibility between the different software and inferior size of the scans.

**Keywords:** laser scanning, point clouds, virtual reality, iPhone 13 Pro, 5<sup>th</sup> generation iPad Pro.

# List of Contents

<i>Abstract</i> .....	<i>i</i>
<i>List of Figures</i> .....	<i>iv</i>
<i>List of Tables</i> .....	<i>vi</i>
<i>Abbreviations</i> .....	<i>vii</i>
<b>1. Introduction</b> .....	<b>1</b>
1.1. Mining History.....	1
1.2. Motivation.....	1
1.3. Objectives.....	2
<b>2. State of the Art and Point Cloud Data Acquisition Review</b> .....	<b>3</b>
2.1. Laser Scanning.....	4
2.1.1. Terrestrial Laser Scanning (Faro Focus S70) .....	4
2.1.2. Terrestrial Laser Scanning (Leica MS60) .....	7
2.1.3. Mobile Laser Scanning (Apple iPhone 13 Pro and Apple iPad Pro) .....	8
<b>3. Case Study</b> .....	<b>12</b>
<b>4. Material and Methods</b> .....	<b>14</b>
4.1. Data Acquisition .....	15
4.1.1. iPhone and iPad.....	16
4.1.2. Faro Focus S70 .....	19
4.1.3. Leica MS60 .....	20
4.2. Data Processing and Creation of VR Models .....	20
4.2.1. Model 1 - iPhone 13 Pro and iPad 5 Pro 3DScannerApp to Unity .....	21
4.2.2. Model 2 and 3 – Faro Focus S70 to Unity .....	22
4.3. Classification of Rock Mass – Q System .....	29
<b>5. Results and Discussion</b> .....	<b>30</b>
5.1. Image Capture Qualitative Comparison .....	31
5.2. Point Clouds and Meshes Quantitative Comparison .....	35
5.3. VR Models .....	39

5.4. Classification of the Rock Mass using the Q System.....	43
6. <i>Conclusions</i> .....	47
<i>Bibliography</i> .....	49

## List of Figures

Figure 1: Faro Focus S70 Laser Scanner. ....	4
Figure 2: Leica MS60 multistation. ....	7
Figure 3: Representation of the principle of functioning of the Time-of-Flight method embedded in the Apple devices. ....	9
Figure 4: iPhone 13 Pro and its camera system in detail. ....	10
Figure 5: 5 <sup>th</sup> generation iPad Pro and its camera system in detail. ....	11
Figure 7: Iberian Pyrite Belt with locations of main ore deposits and geological bodies. ....	12
Figure 8: Satellite image of the concession area and representation of the mineralized zonas on the Neves-Corvo mine. ....	13
Figure 9: Cross-section of the drift S867B3009 obtained in Deswik, with the geological model of the Neves South orebody. ....	13
Figure 6: Workflow conducted to perform the quantitative and qualitative analysis and VR model comparison from the laser scans obtained with the Apple devices, Leica MS60 and Faro Focus S70 ....	15
Figure 10: Toyota Hilux light system used to provide lighting in the performance of the laser scans. ....	16
Figure 11: Diagram of the different functions available to customize the scans using the 3DScannerApp software. ....	17
Figure 12: Representation of the record method (transversal and longitudinal sections) used in the different scans. ....	18
Figure 13: Screenshot of the screen of the Faro Focus S70 Laser Scanner, revealing the scanning setting menus. ....	19
Figure 14: Model creation in each respective model and involved software. ....	21
Figure 15: Import of the iPhone and iPad scans to Unity. ....	22
Figure 16: Process to import a point cloud into the software ReCap Pro. ....	23
Figure 17: Screenshot from CloudCompare demonstrating a section of the point cloud's attributes table. ....	24
Figure 18: Visualization of the point cloud obtained with the TLS method, in the CloudCompare Software. ....	24
Figure 19: Clipped section of the relevant portion of the point cloud obtained with TLS in CloudCompare. ....	25
Figure 20: Configuration of the Poisson Surface Reconstruction parameters in CloudCompare. ....	26
Figure 21: Generated surface using CloudCompare's Poisson Surface Reconstruction function. ....	26
Figure 22: Final surface after filtering the values with the least information, resulting in a mesh with triangles formed only with a high input of vertices. ....	27
Figure 23: Comparison between the point cloud obtained through TLS and the mesh generated from it in CloudCompare. ....	27
Figure 24: Visualization in MeshLab of the mesh generated in CloudCompare. ....	28
Figure 25: Preview of the Faro Focus Scan with Unity. ....	28
Figure 26: Screenshots of the iPhone 13 Pro, showing the models generated by the 3DScannerApp. ....	31

Figure 27: Highlighted details of the model generated with the iPhone 12 Pro, using the 3DScannerApp..	32
Figure 28: Screenshots of the visualization of the drift's laser scan in the software ReCap Pro.	33
Figure 29: Screenshot of RealView in ReCap Pro.	34
Figure 30: Surface density representation of diferente scans.	36
Figure 31: Scheme representing the different resolutions obtained with the Faro Focus (red) and iPhone 13 Pro (Blue).	39
Figure 32: Model 1 preview in Unity Game, consisting of the laser scan and photogrammetry captured with the iPhone 13 Pro.	40
Figure 33: Visualization of Model 2 in Unity Scene.	41
Figure 34: Visualization of Model 3 in Unity Scene..	42
Figure 35: screenshot of the different VR models created using MLS with iPhone 13 Pro and TLS with Faro Focus S70..	42
Figure 36: Clustering results obtained with DSE.	44
Figure 37: Zone of the drift with the highest density of discontinuities..	45
Figure 38: Discontinuities roughness highlighted in the eastwall of the drift and table <sup>40</sup> with the shape of discontinuities with different levels of roughness.	45
Figure 39: Display of the roof of the drift, without any evidence of humidity or water flow.	46
Figure 40: Unwedge simulation of block formation in a 5m x 5m drift, considering the characteristics retrieved from the iPhone 13 Pro scan.	47

## List of Tables

Table 1: Performance specifications of Faro Focus Laser Scanner S70. ....	6
Table 2: Performance specifications of Leica MS60 multistation .....	8
Table 3: Camera specifications of the Apple iPhone 13 Pro. ....	10
Table 4: Camera specifications of the Apple’s 5th generation iPad Pro.....	11
Table 5: Characteristics of each of the four selected scans using the Apple devices.....	18
Table 6: Qualitative Results Summary. ....	35
Table 7: Characteristics of the Leica BLK generated mesh adapted to DeswikCAD. ....	37
Table 8: Characteristics of each of the four meshes generated by scans recorded with the 3DscannerApp.....	37
Table 9: Characterization of the mesh generated in CloudCompare, with the laser scan performed by TLS. ....	38
Table 10: Comparison regarding the number of points, scanned surface area, density of points and resolution obtained with the four different devices utilized. ....	38
Table 11: File sizes of each virtual reality model. ....	42
Table 12: Characterization of the Principal Joint Set Families .....	43
Table 13: Estimated parameters, through the laser scanner captured with the iPhone 13 Pro, used to calculate rock mass quality according to the Q-System.....	46



# Abbreviations

BC	Before Christ
AD	<i>Anno Domini</i>
3D	Three Dimension Domain
LiDAR	Light Detection and Ranging
VR	Virtual Reality
TLS	Terrestrial Laser Scanning
AR	Augmented Reality
HDR	High Dynamic Range
RGB	Red Green Blue
MLS	Mobile Laser Scanning
IPB	Iberian Pyrite Belt
VMS	Volcanogenic Massive Sulfides
N – S	North South
E – W	East West
NW	North West
RQD	Rock Quality Designation
J <sub>n</sub>	Joint Set Number
J <sub>r</sub>	Joint Friction Number
J <sub>a</sub>	Joint Infill
J <sub>w</sub>	Joint Water Reduction Factor
SRF	Stress Reduction Factor
LED	Light Emitting Diode
SD	Secure Digital
SF	Scalar Field
DSE	Discontinuity Set Extractor
UAV	Unmanned Aerial Vehicles

# 1. Introduction

## 1.1. Mining History

Mining has a long history that dates back to ancient civilizations, and has been crucial in influencing human development and igniting industrial revolutions<sup>1</sup>. From the application of fire to break hard rock by the Egyptians since 5 000 BC<sup>2</sup>, to the Chinese invention of the blast furnace around 1 000 AD<sup>1</sup>, culminating with the publication of the first mining technical work, *De Re Metallica* in 1556 in Germany, establishing mining as a field of study<sup>2</sup>. In the fifteenth century explosives were already used in Europe to facilitate the breakage of rock<sup>1</sup>.

Forwarding to the eighteenth century, the industrial revolution, powered by the coal extracted from mines takes place, leading to the development of steam powered lifts, drills and pumps furthering the technological evolution in mining<sup>1</sup>. Alfred Nobel invented dynamite in the nineteenth century resulting in a powerful new method of blasting rock, which is today completely obsolete in modern mines<sup>3</sup>. In the last one hundred years the computer was materialized enabling a boom in processing information, with existing software such as Vulcan<sup>4</sup> and Deswik<sup>5</sup> allowing the complete digitization of geological and mine models. Thanks to this continuous progress of technology, mining engineering has evolved consistently over the centuries, to increase productivity, security and sustainability in the extraction, greatly changing mining techniques over the years<sup>6</sup>.

## 1.2. Motivation

Nowadays, the concept of industry 4.0 reveals a set of high potentials in mining<sup>7</sup> including the integration of robotization, 3D simulations and augmented reality to carry on the evolution of the mining industry and civilization itself.

Among these revolutionary technologies, LiDAR (Light Detection and Ranging)/Laser Scanning (LS) has become a potent instrument that allows for the precise and thorough mapping of underground mines<sup>8</sup>.

LS is a technique that measures two angles (one vertical and one horizontal) and uses laser beams to measure distances to calculate three dimensional point coordinates and collect highly precise information about real-world objects and their surroundings<sup>9</sup>. It is possible to gain detailed spatial knowledge about underground mines and a deeper grasp of its complicated geological and structural properties by applying this cutting-edge approach in the mining industry<sup>10</sup>. Traditional methods for surveying and recording mines frequently rely on time-consuming and error-prone manual techniques that have a limit on the amount of detail they can record. In order to acquire high-resolution 3D data of underground mines, laser scanning technology offers a non-intrusive and effective solution<sup>11</sup> to these problems. Nowadays, some apple smartphones are equipped with this technology, which can lead to a more cost-effective and user-friendly manner of recording 3D data with precision in underground mines<sup>8</sup>.

In addition to facilitating accurate measurements, this technology allows to generate virtual reality (VR) models that simulate the underground environment. These VR models offer an immersive experience for viewing and assessing data<sup>12</sup>. VR models can be used in the mining industry to provide training, simulating the underground environment and leading to a reduction of injuries in this sector<sup>13</sup>. Moreover, the combination of virtual reality

and laser scanning presents a fascinating possibility to transform how mining engineers interact with mine drifts. Engineers may examine, evaluate, and transmit vital information in a more natural and engaging way due to virtual reality's visualization capabilities<sup>12</sup>.

### **1.3. Objectives**

Considering the application of VR models of mine drifts and the novel capability of smartphones to capture accurate 3D data, this study aims to investigate the possibility of collecting 3D data of an underground drift with the iPhone 13 Pro and 5<sup>th</sup> generation iPad Pro and its applicability in retrieving valuable information and creating VR models from the collected data. To achieve this goal three main objectives were defined:

- A comparison of point clouds of the same drift, captured with an iPhone 13 Pro, 5<sup>th</sup> generation iPad Pro, Faro Focus S70 and the mesh used by the Neves-Corvo mining operations in Deswik, captured by a Leica MS60, considering density, resolution, and time consumption parameters.
- A comparison of images captured by iPhone 13 Pro, 5<sup>th</sup> generation iPad Pro and the Faro Focus S70 laser scanner, considering its capability of retrieving valuable geological and geotechnical features such as rock type and installed support.
- Data processing effort to create VR models from the conducted scans and comparison considering its time-effectiveness, immersive experience and computing processing.

Therefore, in this work, the laser scanning capabilities of the iPhone 13 Pro and 5<sup>th</sup> generation iPad Pro are tested as a tool to evaluate geotechnical features of a mine drift, and as a mean to allow mine digitation with the creation of robust VR models.

## 2. State of the Art and Point Cloud Data Acquisition Review

Terrestrial Laser Scanning (TLS) is widely accepted as an effective method for surveying and monitoring geological bodies, since it can create 3D models with details regarding discontinuities, geotechnical indices and physical changes such as mass movements<sup>14</sup>. Nevertheless, this method has its limitations, such as the difficulty in registering small (few mm) deformations, since the range is limited by the mass reflectivity<sup>14</sup> and the high cost of the necessary equipment<sup>15</sup>. The LiDAR sensor introduced by Apple Inc. in 2020 for the iPad Pro and iPhone Pro uses the Time-of-Flight technique to scan objects at a maximum distance of 5 meters<sup>16</sup>, presenting a novel, cost effective and time efficient alternative to established methods of topographic land surveying like TLS and photogrammetry<sup>17</sup>. By combining the high-resolution camera and the LiDAR sensor of the iPhone with mobile apps such as 3D Scanner App, it is possible to obtain satisfactory results for scanning, even in poor light conditions<sup>18</sup>. However, this method has its limitations regarding accuracy and precision of the points captured<sup>19</sup>. Despite the mentioned limitations, the smartphone LiDAR technology is deemed adequate to generate 3D models of underground spaces with the possibility of analyzing geotechnical features such as mapping discontinuities<sup>20</sup> or bigger structures like coastal cliffs in a very time-effective manner<sup>17</sup>. Point Clouds and high-quality images can be combined to create virtual reality models<sup>21</sup>. In the field of architectural heritage the generation of digital environments from 3D surveys allows for a higher level of interactivity with augmented and extended reality for users<sup>22</sup>, moreover, the LiDAR technology in Apple devices can be exploited in this field for expeditious surveys<sup>23</sup>. The field of geosciences is evolving, with an interdisciplinary approach combining video game engines it is now possible to simulate rockfalls and develop virtual reality programs<sup>24</sup>. Most of the development made in the virtual reality or augmented reality (AR) spectrum of geosciences consists in the training of operators or students, eliminating the negative effect of the presence in dangerous areas<sup>25</sup>. The usage of these innovative technologies appears to benefit task accomplishment<sup>26</sup> in remote operations and also students' ability to improve their knowledge<sup>25</sup>.

TLS is already categorized as an effective method to create 3D models of geological bodies with enough detail to assess stability of slopes<sup>14</sup> and when combined with high resolution photography, it can create realistic VR environments<sup>22</sup>. Nevertheless, it is a time-consuming method and requires not only expensive equipment but also trained operators to perform the survey<sup>27</sup>. On the other hand, if the Apple's devices can construct VR models with sufficient detail to assess geological features of a drift, bench or cliff, it allows trainees to develop their knowledge without the dilemmas of distance, costs and risk management, but also enables the possibility of rock mechanics experts to assess the security and overall conditions of a given geological body with a greater immenseness than computer models or just photography, while eliminating the logistical problems mentioned before. And simultaneously, by a lower price and less time when compared with a TLS device, in a more simplistic and user-friendly manner.

## 2.1. Laser Scanning

Laser scanning is now a widely used technique for gathering 3D data. The laser scanner measures the distance from the sensor to the object methodically using laser light. There are several types of laser scanners, depending on the method of measuring distances<sup>16</sup>. Pulse scanners work by sending out a laser pulse that is then reflected off a surface and returned to the receiver. The distance to the reflected surfaces is calculated based on the flight time. With knowledge of the range vector's origin and the scanning angle, the measured distances are converted to 3D coordinates<sup>14</sup>. Phase-based laser scanners calculate the distance to the scanned object by emitting a continuous high intensity wave and comparing the phase difference between the transmitted and received signal, and thus is suitable for shorter range scanning, since the continuous wave is less powerful than the pulse-based ones<sup>25</sup>. Lastly, there are LiDAR devices where the distance is calculated using triangulation methods, by solving plane triangles, relying on the observation of a spot emitted by a laser diode with an optical receiver system<sup>25</sup>, resulting in accuracies in the hundredths of a millimeter, however with a short scanning range in the scale of meters<sup>16</sup>.

### 2.1.1. Terrestrial Laser Scanning (Faro Focus S70)

The equipment used to perform the TLS was the Faro Focus Laser Scanner S70 (Figure 1). These devices are specifically designed for both indoor and outdoor measurements in industries such as Architecture, Engineering, Construction, Public Safety and Forensics or Product Design<sup>28</sup>, allowing the registration of the distances and thus the surface of the scanned area and also the capture of high quality photographs due to its High Dynamic Range (HDR) Camera, resulting in point clouds with realistic RGB coloring<sup>28</sup>.



Figure 1: Faro Focus S70 Laser Scanner<sup>29</sup>.

Furthermore, this equipment relies on the Phase-Shift method of scanning<sup>30</sup>, where a continuous wave is emitted and then the range ( $r$ ) is calculated by comparing the phase difference ( $\Delta\varphi$ ) of the emitted and received signal<sup>31</sup>.

$$r = \frac{\Delta\varphi}{2\pi} \times \frac{\lambda}{2} + \frac{\lambda}{2} \times n. \quad (\text{Equation 1})$$

Where the wavelength is  $\lambda$  in meters, and  $n$  represents the number of full wavelengths between the sensor and the observed object (Equation 1).

The performance specifications of the Faro Focus Laser Scanner S70 are represented in Table 1.

**Table 1: Performance specifications of Faro Focus Laser Scanner S70.** With detail regarding the scanner’s range, range noise, color resolution of high-quality imagery, its’s class and other specifications such as field of view.

<b>CHARACTERISTICS</b>	
	<b>Ranging unit</b>
Unambiguity interval	614m for up to 0.5 mil pts/sec 307m at 1 mil pts/sec
	<b>Range</b>
90% Reflectivity (white) 10% Reflectivity (dark-gray) 2% Reflectivity (black)	0.6 – 70m 0.6 – 70m 0.6 – 50m
	<b>Range noise (mm)</b>
10m at 90% (white) 10m at 10% (dark-gray) 10m at 2% (black) 25m at 90% (white) 25m at 10% (dark-gray) 25m at 2% (black)	0.3 0.4 1.3 0.3 0.5 2.0
	<b>Other specifications</b>
Max. measurement speed (mil. Pts/sec) Ranging error (mm) Angular accuracy 3D point accuracy	Up to 1 +/- 1 19 arcsec for vertical/horizontal angles 2 at 10m and 3.5 at 25m
Color resolution	Up to 165-megapixel color
HDR Camera	Exposure bracketing 2x, 3x, 5x
Parallax	Minimized due to co-axial design
Field of view	300° vertical and 360° horizontal
Max Scan Speed	97Hz
Laser Class	1
Wavelength	1550nm
Data storage	SDHCTM, SDXCTM, 32GB; max. 512GB card
Scanner control	Via touch screen display and WLAN connection, Access by mobile devices with HTML5
WLAN	Via touch screen display and WLAN connection, Access by mobile devices with HTML5

Considering its high-quality measurement capability<sup>28</sup> and wide acceptance as an effective method to survey geological bodies<sup>14</sup>, the data obtained with this equipment will be considered the base upon which the mobile

laser scanning (MLS) data gathered through Apple devices will be compared to measure and understand its applicability in the field of the geological sciences.

### **2.1.2. Terrestrial Laser Scanning (Leica MS60)**

Similar to the Faro laser scanner, Leica MS60 (Figure 2) is a scanning tool used in construction and mining<sup>32</sup>, relying on the phase-shift method of laser scanning<sup>32</sup>. This device is equipped with a telescope and overview cameras allowing the capture of high-resolution images<sup>32</sup>.



**Figure 2: Leica MS60 multistation<sup>32</sup>.**

The Leica MS60 multistation is currently the device used by the Neves-Corvo topography team to collect routine point-measurements of the mine's drifts and developments. In table 2, it is described the performance characteristics of the Leica MS60.



**Table 2: Performance specifications of Leica MS60 multistation<sup>32</sup>.** With detail regarding the scanner’s range, range noise, color resolution of high-quality imagery, its’s class and other specifications such as angular accuracy.

<b>CHARACTERISTICS</b>	
	<b>Working range (m)</b>
Distance Accuracy	5 – 150 0.05 at 100
	<b>Maximum Range (m)</b>
30kHz mode 8kHz mode 1kHz mode 1kHz mode	60 150 300 1 000
	<b>Range noise (mm)</b>
30kHz mode 8kHz mode 1kHz mode 1kHz mode	3.0 1.5 1.0 0.6
	<b>Other specifications</b>
Max. measurement speed (1000 Pts/sec) Angular accuracy	30 1''
Color resolution	Two 5 megapixel digital cameras
Overview Camera zoom Telescope Camera magnification/ zoom	8x zoom 8x zoom, 30x optical magnification
Scan Rate	30 000 Hz
Laser Class	2

### **2.1.3. Mobile Laser Scanning (Apple iPhone 13 Pro and Apple iPad Pro)**

Apple introduced in 2020 its first products with LiDAR technology, the 4<sup>th</sup> generation iPad Pro and 12<sup>th</sup> generation iPhone Pro and Pro Max<sup>33</sup>. These devices utilize the Time-of-Flight method to perform laser scanning, revealing what could be a disruptive alternative to the already established topographic surveying methods<sup>17</sup>. This laser scanning method relies on calculating the distance ( $D$ ) between the observed object and the scanner by dividing by two the speed of the light beam ( $C$ ) and multiplying by the time ( $\Delta t$ ) it took from emitting until receiving the signal (Equation 2)<sup>31</sup>.

$$D = \frac{C}{2} \times \Delta t \quad (\text{Equation 2})$$

Figure 3 depicts the principle that is implemented in the Time-of-Flight scanning method that is integrated in the Apple devices. The transmitter emits a laser beam until it reaches the target, being this the object to be scanned, located at a distance of  $D/2$ . Afterwards, the laser beam is reflected and captured by the receiver, and by knowing the speed of light and the time it took to cross a distance of  $D$ , it is possible to calculate the position of the target<sup>31</sup>.

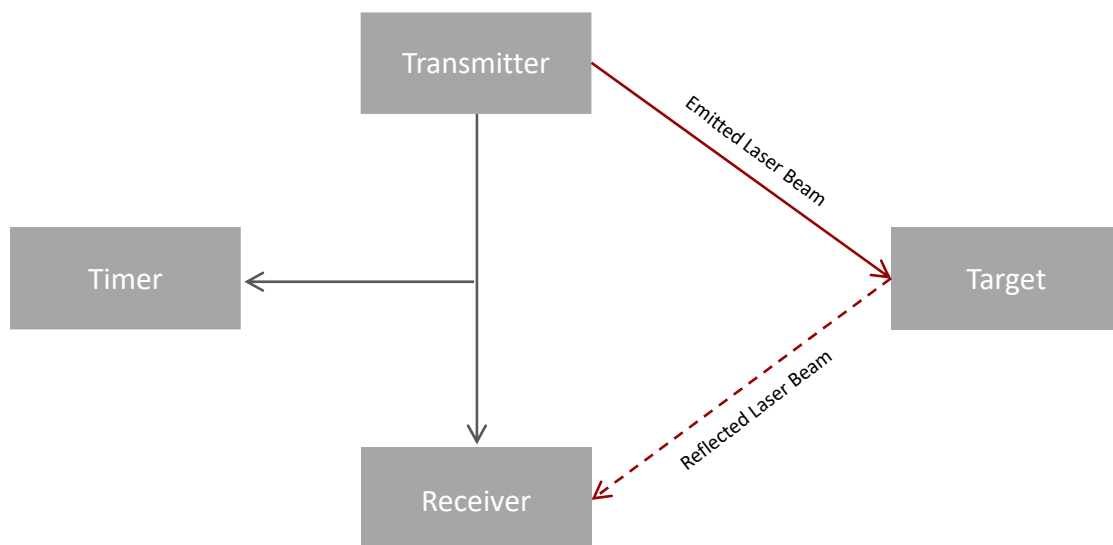


**Figure 3: Representation of the principle of functioning of the Time-of-Flight method embedded in the Apple devices.** The transmitter and receiver embedded in the device’s LiDAR sensor, transmit the beam, and capture the reflected light of the target, respectively. Then, through the device’s timer the interval of time between the emission of the beam and its reception is calculated, allowing for the estimation of the position of the target<sup>31</sup>.

In this study the devices used were the iPhone 13 Pro and the 5<sup>th</sup> generation Apple iPad Pro.

The iPhone 13 Pro is an Apple smartphone released in September 2021, with a Pro 12MP camera system consisting of three different cameras: Telephoto, Wide and Ultra Wide<sup>34</sup>, the American company stated that this resulted in “A dramatically more powerful camera system”, coupled with a LiDAR Scanner to, according to the maker, enable night portraits. But consequently, with the aid of already developed apps such as 3DScannerApp it enables the capture and creation of 3D models through laser scanning<sup>35</sup>. Figure 4 represents the iPhone 13 Pro device and the components of its camera system, while Table 3 details its camera specifications.

**Table 3: Camera specifications of the Apple iPhone 13 Pro.** With detail regarding the different apertures of the three cameras, the zoom capacity and image stabilization<sup>34</sup>.

PRO 12MP CAMERA SYSTEM CHARACTERISTICS	
	Aperture (f/stop)
Telephoto	2.8
Wide	1.5
Ultra Wide	1.8
Optical zoom in Optical zoom out Optical zoom range	3x 2x 6x
Other characteristics	Details
	Dual optical image stabilization (Telephoto and Wide) Sensor-shift optical image stabilization (Wide) Smart HDR 4



**Figure 4: iPhone 13 Pro and its camera system in detail<sup>34</sup>.** The device presents a camera system with three different cameras allowing for an advanced image stabilization and several aperture ranges. Furthermore, the smartphone is equipped with a regular flashlight and a LiDAR Sensor, enabling the performance of laser scanning.

The other Apple device tested in this dissertation was the 5<sup>th</sup> generation iPad Pro, which likewise the mentioned smartphone, was released in the year 2021<sup>34</sup>. This tablet's camera system specifications are described in Table 4.

**Table 4: Camera specifications of the Apple’s 5th generation iPad Pro<sup>34</sup>.** With detail regarding the different apertures of the two cameras, the zoom capacity and image stabilization.

PRO CAMERA SYSTEM CHARACTERISTICS	
	Aperture (f/stop)
Wide (12MP)	1.8
Ultra Wide (10MP)	2.4
Optical zoom out Digital zoom up to	2x 5x
Other characteristics	Details
	Auto image stabilization Lens correction stabilization (Ultra Wide) Smart HDR 3

In comparison with the Apple iPhone 13 Pro’s camera system, this camera system features one less camera (Telephoto) and the Wide and Ultra Wide cameras present a higher aperture, which translates into less light being captured by the camera<sup>36</sup>, which can be problematic considering the data acquisition will be performed in an underground environment with only artificial lighting. Moreover, the HDR in the iPad is inferior, resulting in a more reduced range of colors. Figure 5 illustrates the camera system available in the 5<sup>th</sup> generation iPad pro.



**Figure 5: 5<sup>th</sup> generation iPad Pro and its camera system in detail<sup>34</sup>.** This camera system consists of two cameras (Wide with a resolution of 12MP and Ultra Wide with 10MP), permitting also image stabilization and lens correction<sup>34</sup>. Likewise the iPhone 13 Pro, the device is equipped with the flashlight and LiDAR Sensor, also allowing this device to perform laser scanning<sup>33</sup>.

### 3. Case Study

The data acquisition for this study took place in the Neves Corvo mine in Castro Verde, Portugal. This mine is located in the Iberian Pyrite Belt (IPB), which consists in a province of volcanogenic massive sulfides (VMS) deposits, extending roughly 250km in length and 50km in width from Grândola, Portugal to Sevilla, Spain<sup>44</sup>. With an orientation approximated to N-S and culminating in E-W, respectively<sup>44</sup>. This geological setting is represented in Figure 7.

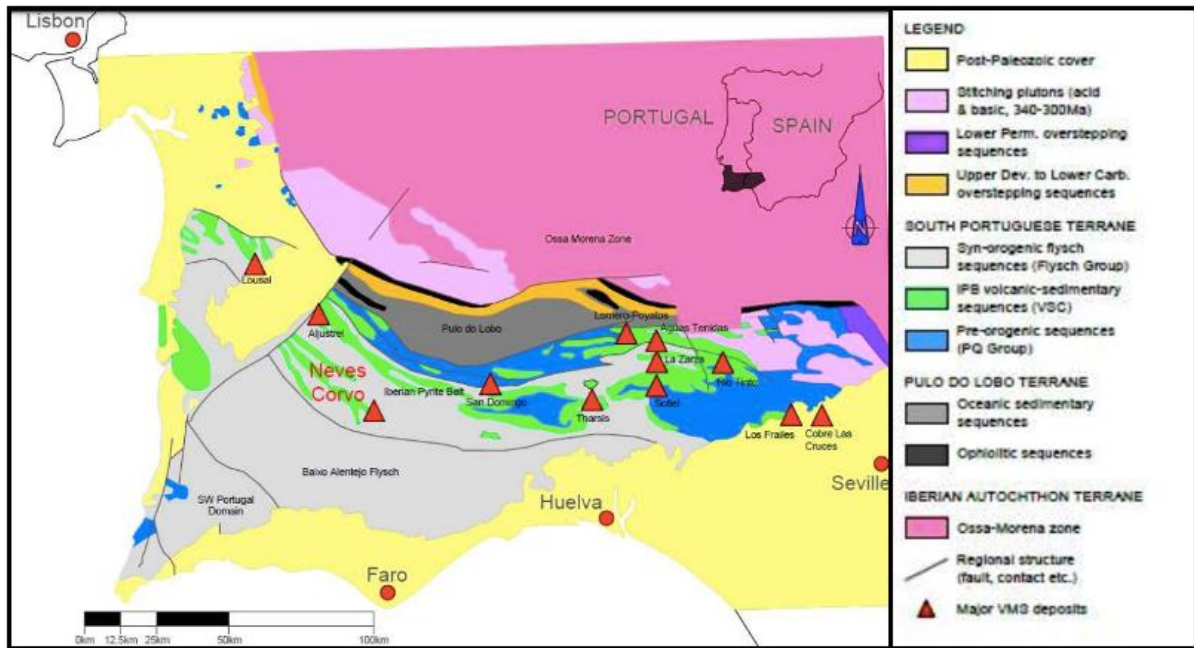


**Figure 7: Iberian Pyrite Belt with locations of main ore deposits and geological bodies<sup>45</sup>. The Neves-Corvo mine is located in the south-Portuguese terrane, consisted of the Flysch Group, the IPB volcanic-sedimentary sequences and the Pre-Orogenic sequences.**

Despite the similarities with other deposits in the IPB, Neves-Corvo high copper grades and strong metallic zonality make it a unique deposit<sup>46</sup>. Currently exploring zinc, copper and lead. The mine comprehends five different ore bodies: Neves; Corvo; Graça; Zambujal and Lombador<sup>45</sup>. Their location is represented in plane view in Figure 8.

These orebodies are lenticular-shaped and composed of massive sulfides including pyrite, chalcopyrite, sphalerite, galena and other sulfides<sup>46</sup>.

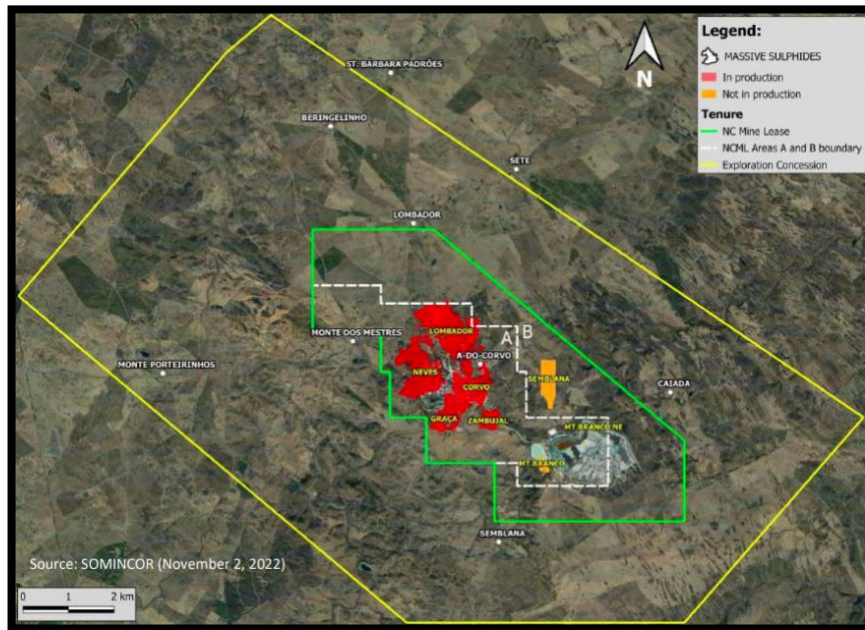


**Figure 8: Satellite image of the concession area and representation of the mineralized zonas on the Neves-Corvo mine<sup>45</sup>.** The yellow line represents the limits of the exploration concession, whereas the green line the mine lease. The orebodies in production are represented in red while the orebodies not in production in orange.

The data acquisition took place in the Neves ore body, more specifically in the drift S867B3009, located approximately 333 meters underground, in the Neves South section. This orebody with its longest axis of 1200m oriented to NW, thickness of maximum 55m and average width of 700m, is characterized as subhorizontal with an average inclination between 5° and 15°<sup>46</sup>.

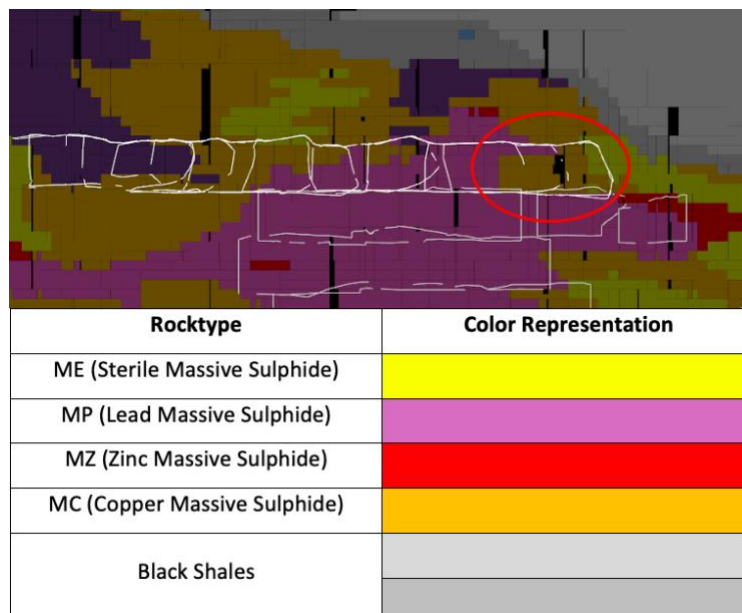


**Figure 9: Cross-section of the drift S867B3009 obtained in Deswik, with the geological model of the Neves South orebody.** The scanned area is highlighted with the red circumference.

Figure 9 represents a cross section of the drift used as the case study, with the geological model in Deswik. The color scheme represents the different lithologies by ore grade present in this mineral mass, and thus it is possible to classify the drifts rock types, such as ME which represents massive sulphide with copper and zinc grades below the cutoff grade.

## 4. Material and Methods

In order to develop this study, laser scans of the mine drift S867B3009 were conducted using the following devices: Apple iPhone 13 Pro, 5<sup>th</sup> generation Apple iPad Pro, Faro Focus S70 and Leica MS60, the latter used by the topography team of the Neves-Corvo mine.

A qualitative and quantitative comparison was performed considering the point clouds and the meshes, since it is possible to take into consideration the vertices and the created faces from the vertices. These outputs are compared regarding its number, the scanned area and consequently the generated density and resolution obtained with each scan.

Resolution is defined as the average distance between two points in a point cloud, or as the point density of the cloud<sup>37</sup>. Hence, the resolution value (*Res*) of each laser scan can be calculated (Equation 5) as the square root of the division of the area of the surface captured ( $S_A$ ) by the number of points of the point clouds ( $P$ ), resulting in the average distance between two points in the point cloud.

$$Res = \sqrt{\frac{S_A}{P}} \quad (\text{Equation 5})$$

As a comparison metric, this study also considers the surface density, which equals the number of neighbors ( $N$ ) of a point, divided by the neighborhood surface ( $\pi r^2$ ), defined as a sphere of radius  $r$ <sup>38</sup>. As depicted in the Equation 6:

$$SD = \frac{N}{\pi r^2} \quad (\text{Equation 6})$$

Furthermore, considering the apple devices and the faro focus laser scanner ability to capture images, these were compared regarding its capacity to display geological and geotechnical features such as the color of the rock mass, the support installed, the existence of alteration in the support and rock and the characterization of discontinuities.

The scans performed with the iPhone 13 Pro and the Faro Focus S70 laser scanner were processed into Unity, allowing the creation of Virtual Reality models. These models are tested and compared regarding the user-friendliness of their creation and the ability to recreate the drift environment. Moreover, the scanning conducted with the iPhone 13 Pro was used to classify the present rock mass following the Q-System, by defining joint set families with the freeware Discontinuity Set Extractor (DSE v210, 2024).

Figure 6 describes the workflow conducted in this study to produce the quantitative analysis of the point clouds and meshes, the qualitative analysis of the images captured with the scans, the comparison of the VR models and the rock mass classification from the iPhone laser scan.

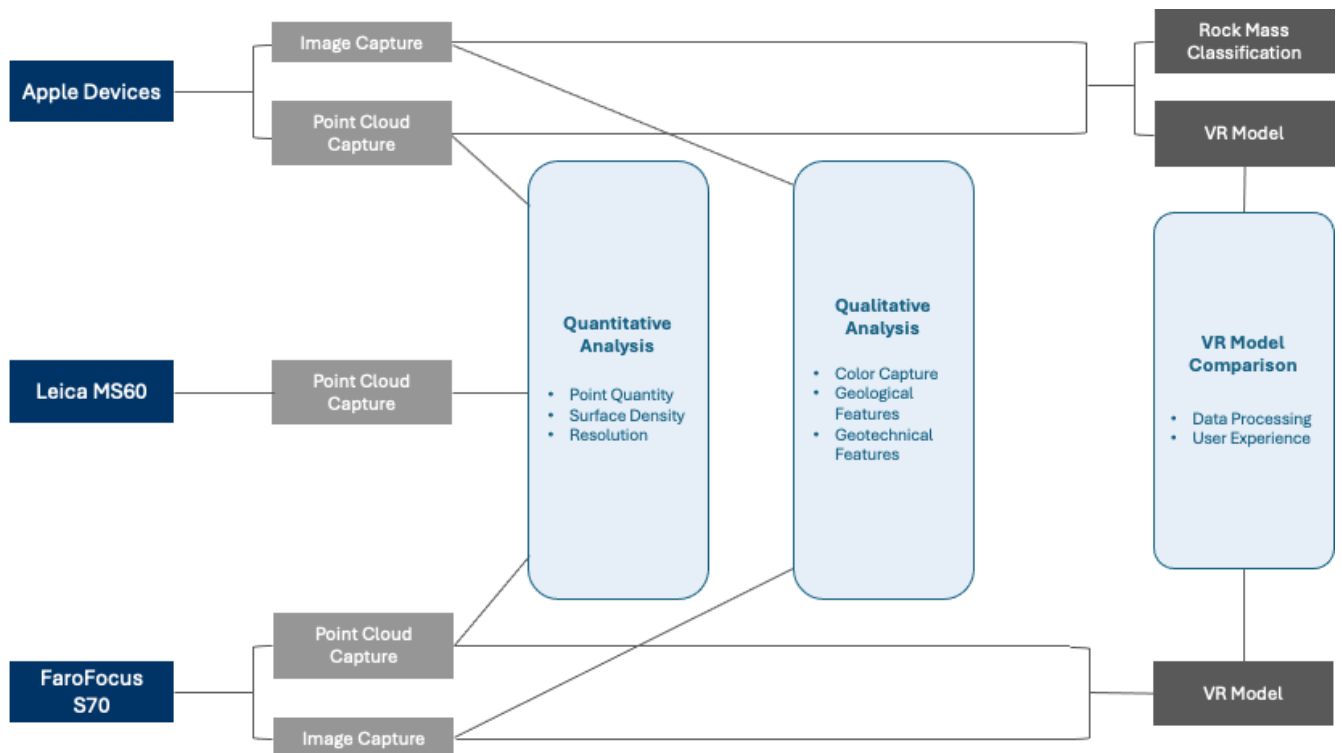


**Figure 6: Workflow conducted to perform the quantitative and qualitative analysis and VR model comparison from the laser scans obtained with the Apple devices, Leica MS60 and Faro Focus S70**

#### 4.1. Data Acquisition

The data collection took place in the drift S867B3009 in the Neves-Corvo mine, on 27<sup>th</sup> of April 2023. Considering the underground environment, the only light source used to perform the trials were the lights of the Somincor vehicle VT-916, Toyota Hilux. It’s lighting system, shown in Figure 10, consists of the car headlights, an extra LED light projector located on the top of the vehicle and two amber warning lights, which were always kept on due to security policy reasons.





**Figure 10: Toyota Hilux light system used to provide lighting in the performance of the laser scans.**

During the recordings, all the headlights of the vehicle and the LED light projector were turned on to provide a light source for scan performance, which consists of the laser scanning itself and the capture of high-quality images. Moreover, the amber warning lights were also kept on, since it is mandatory in the underground environment of Neves-Corvo.

#### **4.1.1. iPhone and iPad**

Despite being equipped with a LiDAR system, to conduct a laser scan of an object with the iPhone 13 Pro or the 5<sup>th</sup> generation iPad Pro it is necessary to install a specific application for this purpose<sup>17</sup>, the one utilized in this study was the 3DScannerApp. It is noteworthy to mention that this software is only available for smartphones with OS systems, more specifically for iPhone, iPad and iPod iOS 14.0 or later and for MacBook macOS 12.0 or later<sup>34</sup>.

Upon installation, the software is very intuitive. Having a simple menu (Figure 11) to setup the scan with the optimal configurations. Due to the nature of this study, the chosen resolution was high, and afterwards different characteristics were implemented to optimize the results.

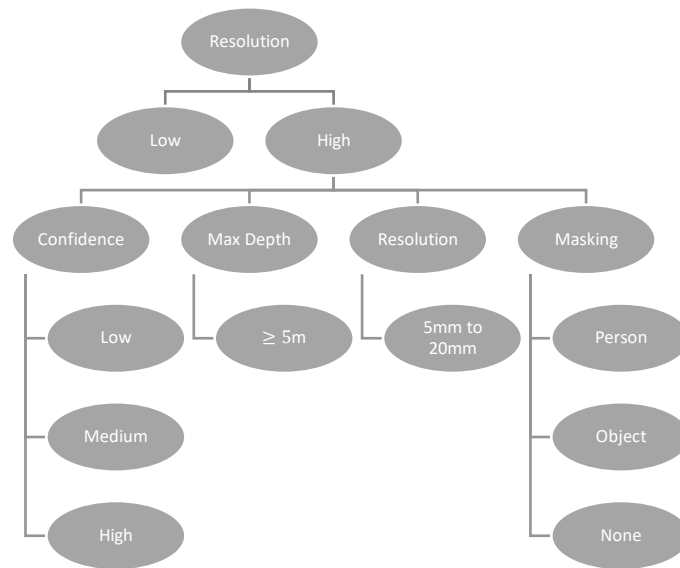


**Figure 11: Diagram of the different functions available to customize the scans using the 3DScannerApp software<sup>42</sup>.** The application displays a menu with options allowing users to custom the scans to the best suitable option for their specific purpose. Starting by defining the type of resolution wanted, being then possible to specify the confidence level, the depth of the target, the specific resolution required and what is the target to scan.

Considering these high-resolution options, confidence is defined to act as a threshold for the data incoming from the sensor. Thus, by choosing High Confidence the scan will only record the highest quality data, reducing the amount of data available<sup>47</sup>. The Max Depth function discards the captured data after the defined distance<sup>47</sup>, and considering a literature review, the optimal distance from which the scan can capture valuable points is determined to be 5 meters<sup>17</sup>. The resolution option can be defined from 5mm to 20mm and defines the accuracy of the scan<sup>47</sup>, hence low values lead to a higher accuracy but limit the scanned area, due to the file size. At last, the masking functionality is intended to isolate the object or person being scanned<sup>47</sup>.

Several scans were conducted, using different customizations and recording methods, being noted that by setting the resolution lower than 20mm was counter-productive, resulting in files too large to process or scan the intended area. Furthermore, the high-resolution lead to a loss of quality in the scans due to an increased difficulty in correctly locating the points, resulting in large “holes” without information in the generated models. Due to this, only four scans were considered, with the settings described in Table 5.

**Table 5: Characteristics of each of the four selected scans using the Apple devices.** In the table is shown the device used to capture each scan, and the setting selected regarding the confidence, resolution, maximum depth and masking. It is also displayed the recording method implemented and the resulting scan size of the file.

Scan	Device	Confidence	Resolution	Max Depth	Masking	Recording Method	File Size
1	5 <sup>th</sup> Generation iPad Pro	High	20mm	5m	None	Longitudinal Sections	187642 KB
2	iPhone Pro 13	High	20mm	5m	None	Transversal Sections	301627 KB
3	5 <sup>th</sup> Generation iPad Pro	High	20mm	5m	None	Transversal Sections	189883 KB
4	iPhone Pro 13	High	20mm	5m	None	Longitudinal Sections	321499 KB

Table 5 demonstrates that despite using the same customizations, the result between the two different devices varies in terms of the size of the mesh, ranging from 1.59 to 1.71 times bigger when scanned with the iPhone rather than the iPad. Moreover, within the same device the file sizes vary with the scan being recorded with a different method. Nevertheless, these small variations should be ignored since they are below 10% and the scanned area is not exactly the same for each scan. Figure 12 exemplifies the two applied methods of recording the laser scans, A) exemplifies scanning with transversal sections, where the operator holding the iPhone or iPad in the hands, performed transversal loops with close to constant speed, sweeping the area while walking backwards. B) exemplifies scanning by recording with longitudinal sections, where the operator held the device and swept the area by walking with constant speed in the direction of the gallery back and forth, and each time raising the device to scan the entire area.

Each scan consisted of a length roughly of 13 meters from the end of the drift and took approximately 2 minutes to record.

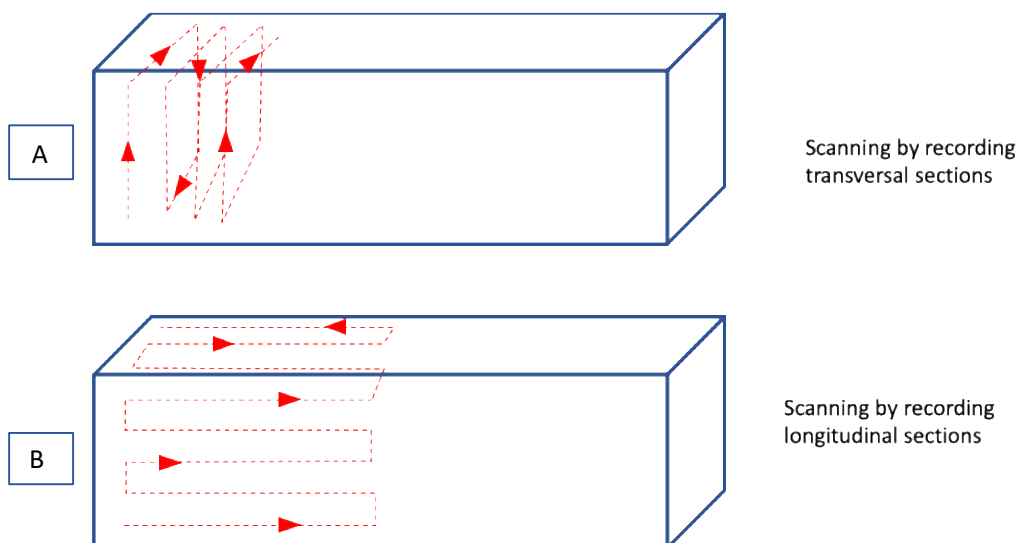


**Figure 12: Representation of the record method (transversal and longitudinal sections) used in the different scans.** The polygon represents the mine's drift, and the red line represents the movement of the device in the operator's hands.

After having successfully created the laser scans with a desired outcome, the application offers the possibility to export the scans in a wide variety of 3D formats<sup>47</sup>. Considering that these scans were intended to further be processed in other software, including Unity, the chosen 3D export format was .obj. This process allows for a quantitative review of the generated meshes, to access the quality of this surveying technique, coupled with the qualitative analysis previously highlighted.

#### 4.1.2. Faro Focus S70

To conduct the measurements using the Faro Focus S70, the lighting source remained the same as for the previous scans, and the laser scanner was placed on top of a tripod, approximately 10 meters from the edge of the drift.

Firstly, the laser scanner was turned on, resulting in a flashing blue light, once the light was stable, the scanner was ready. Afterwards the intended units of length and temperature for the measurement were set, followed by specifying the scanning details and parameters, such as the scan name, the resolution, orientation and colors settings (Figure 13).

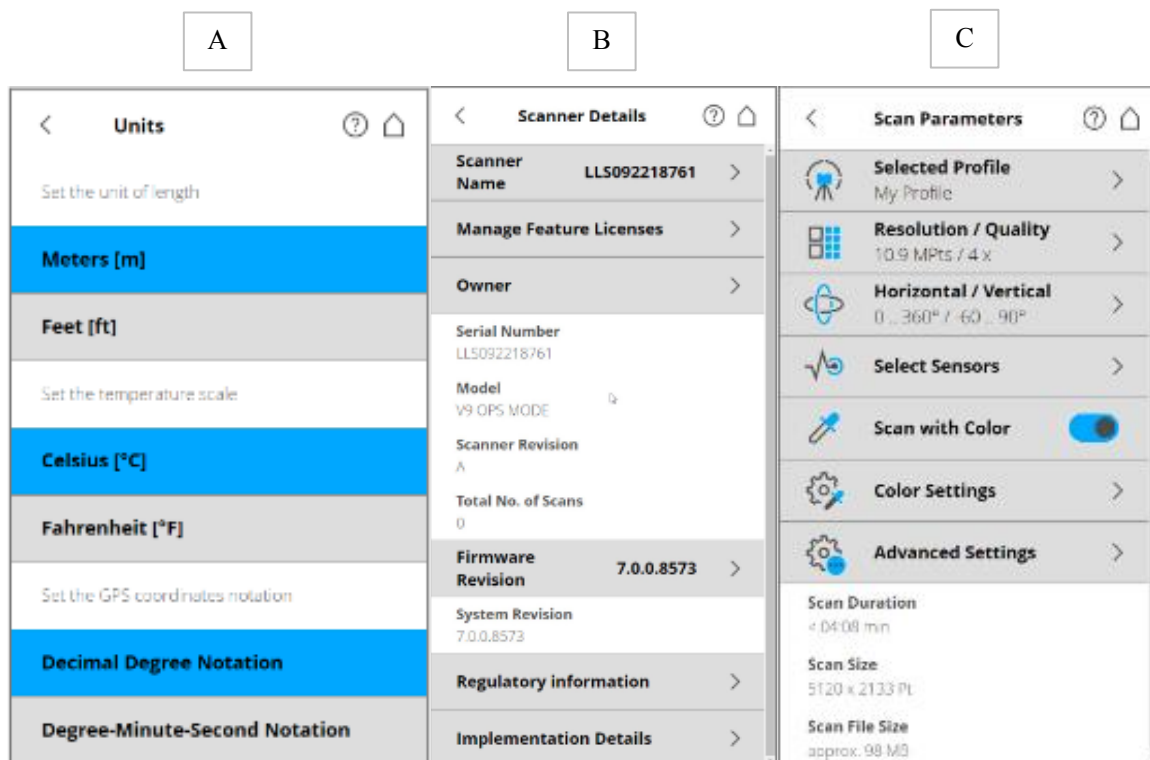


**Figure 13: Screenshot of the screen of the Faro Focus S70 Laser Scanner, revealing the scanning setting menus. A) shows the menu to set the units of the scan, B) the scanner specifications and C) the scan parameters such as to scan with color. Once the desired settings are all set, one can commence the scan by clicking “start scan”.**

In total two scans were conducted, each one took approximately 10 minutes to be completed, and after completion these were saved in a SD card previously inserted in the laser scanner. After scanning, it was possible

to view the scan in a gray-scale picture, allowing the confirmation of the capture of the desired objects. The scans were exported to the SD card in the .fls format, which is a point cloud format specific to the Faro system.

#### **4.1.3. Leica MS60**

The topography team in the Neves-Corvo mine performed a laser scan using the TLS method of the same drift, with the Leica MS60 multistation. This type of data collection is an integral part of the mining cycle, as this data is afterwards integrated in the Deswik files allowing volume and development estimation and geometrical assessments.

To perform this scanning the topographers stationed the device and its tripod in the drift, used the device to read two known points, georeferencing the location. Afterwards the Leica MS60 specifications were selected to capture a point cloud in a mesh of 50cm by 50cm, since this resolution is considered sufficient for the routine surveying of the drifts and prevents the files from becoming too heavy, allowing their integration to Deswik. This type of survey takes about 5 minutes to perform.

Afterwards, the point cloud was processed in the software cyclone to remove the noise and furthered included into Deswik as a mesh. The processed mesh already inserted in Deswik was the one considered in this study.

## **4.2. Data Processing and Creation of VR Models**

With scans of acceptable detail obtained with the different capturing techniques, the creation of Virtual Reality models of the mine drift was conducted. With these models, it is possible to assess the effect of immersion in collecting visual information *ex situ* via VR models, rather than through a computer monitor, and simultaneously evaluate the capability and potential of designing VR models of mines from scans obtained of real underground environments with different methods.

In this study three VR models were created, one consisting of the scan 2, obtained with the iPhone 13 Pro (model 1), and two consisting of the scan obtained with TLS, using the Faro Focus S70 laser scanner, with the original mesh generated in CloudCompare (model 2) and with a *lowpoly* mesh computed in Blender from the mesh of CloudCompare (model 3), in order to reduce the size and thus computer power needed to process it. The process of VR model construction, including used software, from the scans obtained with iPhone 13 Pro (model 1) and Faro Focus S70 (models 2 and 3) is described in Figure 14.

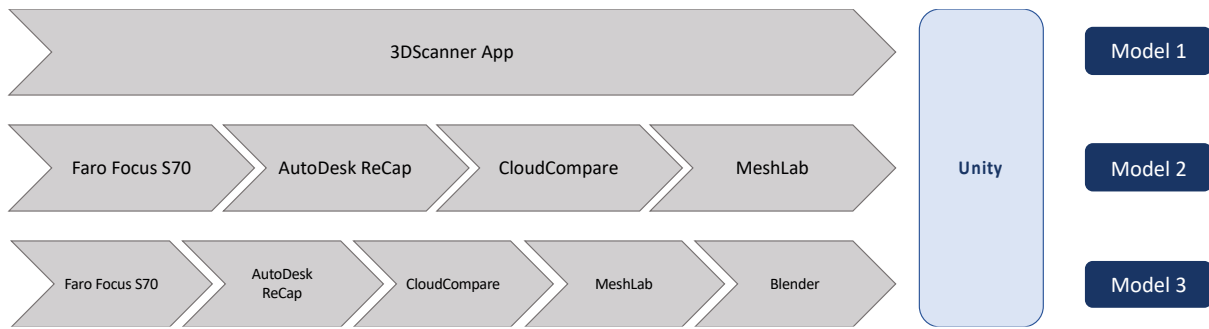


**Figure 14: Model creation in each respective model and involved software.** In order to construct model 3 the scan is first taken with Faro Focus S70, then transformed into a .pts point cloud in AutoDesk ReCap, afterwards into an .ply mesh using CloudCompare and converted in a .dae mesh in MeshLab, with the final step being the low-poly process in Blender to diminish the memory space, before importing to Unity. The chain process utilized for model 2 consists of the same steps of model 3, skipping the processing in Blender. The simpler algorithm consists of the one to create model 1. Where the scan is taken in the application 3DScanner App, exported in .obj as a mesh and the texture exported in the .jpg file, being both directly imported into Unity.

#### 4.2.1. Model 1 - iPhone 13 Pro and iPad 5 Pro 3DScannerApp to Unity

Considering that the 3DScannerApp offers a wide array of exporting formats<sup>47</sup>, the process of importing the scans to a virtual reality creation software becomes quite straightforward. In this study, the utilized software was Unity (Unity 1.23f1, 2022), due to being a free software with a high degree of available information regarding the creation of VR models with considerate user friendliness.

By having the scans stored on the device, they were directly imported to the Unity scene by going to the *Assets* menu, selecting *import new asset* and afterwards selecting the file to be imported. As depicted in Figure 15, the scan appeared in the Unity scene without any color or texture, this can be advantageous to quickly examine the scan to assess its quality regarding the existence of unscanned areas, as already seen in the 3DScannerApp. Considering the goals of this study, was important to visualize the real colors of the scans, since they can provide useful information regarding the geomechanical characteristics of the scanned area. The 3DScannerApp saves the texture of the scans as a .jpg file, which is compatible with Unity. To visualize the scans with its color, was necessary to import the .jpg file as an *asset* and assigned the .jpg file as the texture of the 3D object. This was done by creating a material, appointing the .jpg file as the texture of that material, and then simply dragging the material on top of the 3D object.

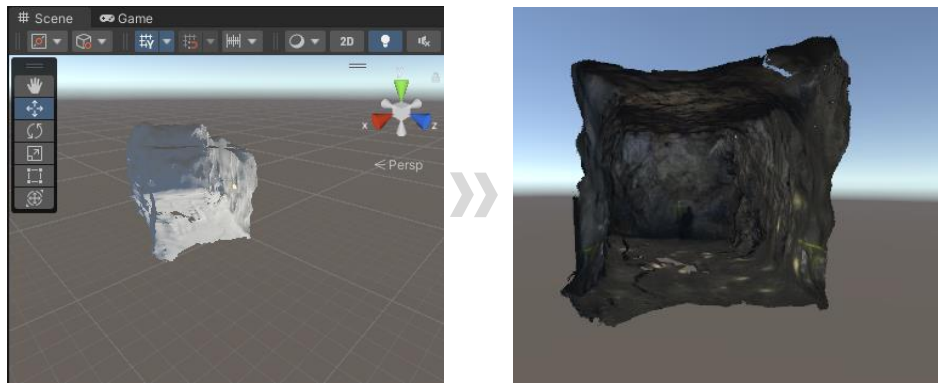


**Figure 15: Import of the iPhone and iPad scans to Unity.** The scan appeared in the Unity scene without any color or texture, by uploading the texture file the 3D object was then previewed with its colors, as already viewed in the 3DScannerApp. By having the scan as intended in the Unity scene, with its texture or color and dimensions preserved, the data processing stage was finished, and it was possible to create a VR model with this object.

By installing the free Unity XR Toolkit plugin the introduction of virtual hands was conducted, mimicking the movements of the controllers, enabling the camera to be located in the level of the user's eyes through the VR glasses and providing the user with free continuous movement<sup>48</sup>. These features allied with the creation of a plane in the floor level for the user to walk on, enable the necessary requirements for the creation of a VR model of the mine drift. Allowing the user to walk in the gallery while seeing it and being able to focus on different points of the tunnel.

#### 4.2.2. Model 2 and 3 – Faro Focus S70 to Unity

Considering that one of the goals of the study consisted in creating VR models from the obtained point clouds, the data processing of the scans taken with the Faro device required a more arduous procedure to ensure compatibility of these scans with the VR creation software. Due to the files format divergency, the process of creating a VR model from a scan captured with a Faro Focus S70 laser scanner is more time consuming, involving different software until the successful import of the scan to Unity without losing important information such as color and texture is possible.

Firstly, the scans were stored *in situ*, in a SD card inserted in the Faro Focus S70. The equipment saves the point clouds in the .fls format, specific of the brand, which is compatible with the Autodesk software ReCap Pro (ReCap Pro v23.1.0, 2023). Hence, the first step of the data processing was to convert the data to a file format compatible with open-source software, using ReCap Pro. As shown in Figure 16, once the software was open, it was necessary to create a new project and import the point cloud, or point clouds to the project, afterwards the software required the definition of the project name and the extension to where the files would be stored.

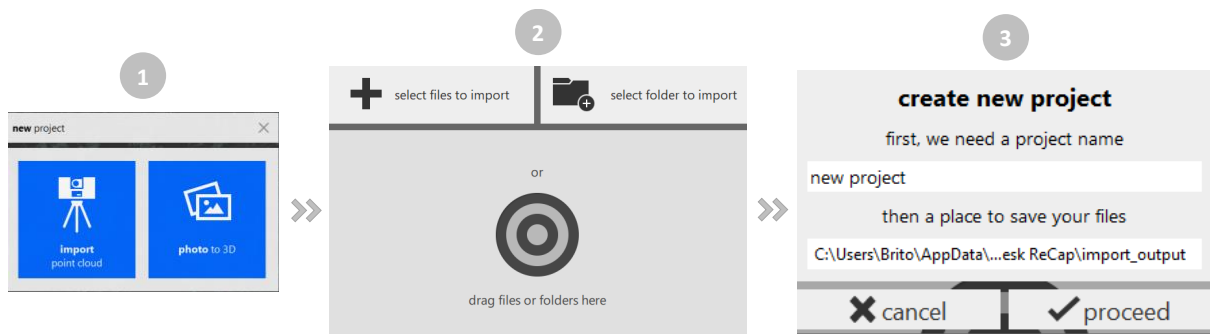


**Figure 16: Process to import a point cloud into the software ReCap Pro.** Firstly it was necessary to choose “import point cloud”, afterwards the file was dragged to the area depicted in point 2 and then it was necessary to name the project.

Subsequently, the point cloud was visible in the screen, allowing for a detailed visualization of the results of the scan, from different points of view including the one from where the scanner was placed, and the measurement of distances between diverse points.

Following the inspection of the scan, to convert it to a different type of format it was necessary to export it and chose the file type between rcp, pts and e57, in this study the .pts format was selected due to its compatibility with other software and other file types such as .txt. This type of file could be converted to a .txt by simply changing its name.

Afterwards, the output of the ReCap Pro was used as the input in CloudCompare (CloudCompare v2.13, 2022). When importing the point cloud some adjustments in the file were needed in order to conserve the color properties. The exported file from ReCap consists in a matrix where the first line is the number of vertices and each of the subsequent lines correspond to vertices, whereas the columns are the properties in the following order: X coordinate, Y coordinate, Z coordinate, Red, Green, Blue, Reflectance, Normal X, Normal Y and Normal Z. To correctly open the file, without losing any properties of the points, it was necessary to delete the first line and swap the column order to the following: X coordinate, Y coordinate, Z coordinate, Grey (this provides the color scale), Red, Green, Blue, Normal X, Normal Y, Normal Z, as depicted in the Figure 17. Since the input consisted in a .pts file, the prior conversion into a .txt file was needed, afterwards these adjustments were made manually before importing it to CloudCompare, since this program can also open .txt files.



Open Ascii File

Source: C:/Users/Brito/Documents/scanteste225112023.pts

Choose an attribute for each column:

Header: 16995585

1	2	3	4	5	6	7	8	9	10
coord. X	coord. Y	coord. Z	Grey	Red (0-255)	Green (0-255)	Blue (0-255)	Nx	Ny	Nz
2.919171	-5.442983	-41.956371	135	131	127	92	-0.475549	0.181074	-0.860852
3.095812	-4.689552	-42.70719	141	174	163	171	0.03183	0.810585	-0.584756
2.66886	-4.349875	-41.88835	189	70	69	51	-0.268604	0.347079	-0.898548
2.378072	-5.45131	-41.864354	141	75	56	60	0.031756	0.109859	-0.99344
1.95458	-4.998883	-41.895478	148	16	39	19	-0.470457	0.262844	-0.842367
3.149546	-3.968187	-43.290941	69	125	119	123	-0.991259	0.125612	-0.040351
2.769504	-3.563506	-41.941911	165	201	184	200	-0.26475	-0.349116	-0.898902
2.743477	-4.471679	-41.915053	194	168	171	162	-0.155479	0.182322	-0.970868
1.559604	-4.784909	-41.999574	106	142	153	139	0.509272	-0.018455	-0.860408
3.043418	-4.881055	-42.238176	150	73	63	51	-0.988787	0.003322	-0.149294
2.940378	-4.228043	-41.9893	218	117	104	95	-0.731766	-0.065137	-0.678436

Separator: (ASCII code: 32) whitespace

Skip lines: 1

Max number of points per cloud: 2000.00 Million

Buttons: Apply, Apply all, Cancel

**Figure 17: Screenshot from CloudCompare demonstrating a section of the point cloud's attributes table.** Each line of the table refers to a point from the point cloud, and each column consists of the different attributes each point has, being this an x, y and z coordinate, the reflectance (which in this software the appropriate is a scale of greys), red, green and blue color value and an x, y and z normal, indicating the direction of the points in the point cloud.

With the file in the desired format and ordination, after clicking *Apply* the software opened the point cloud and the scan became visible in CloudCompare software, while maintaining the scale. Figure 18 demonstrates that by opening the scan in this software it is possible to visualize the same point cloud as in ReCap Pro without visible alterations.

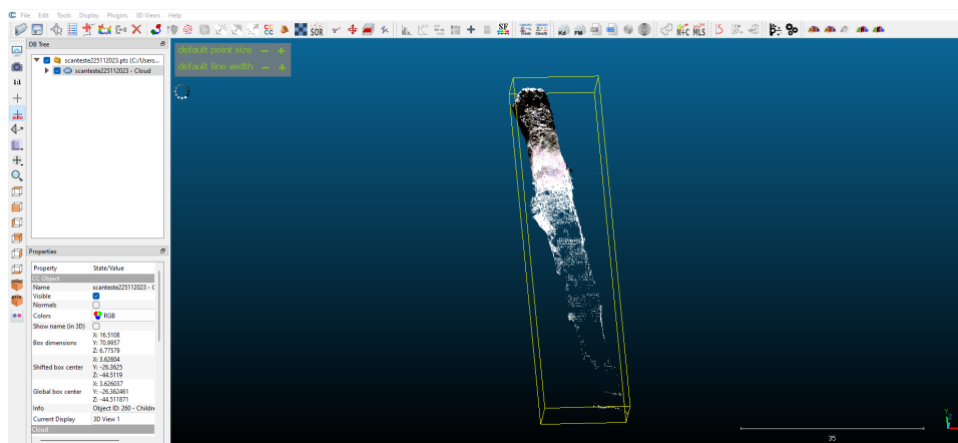


**Figure 18: Visualization of the point cloud obtained with the TLS method, in the CloudCompare Software.**

Considering that this is a rather large file and that some of the collected information is not necessary to conduct the study, the scissor function of the software was used to remove the areas that were not considered, remaining only with the more detailed and point-dense region of the cloud (Figure 19).

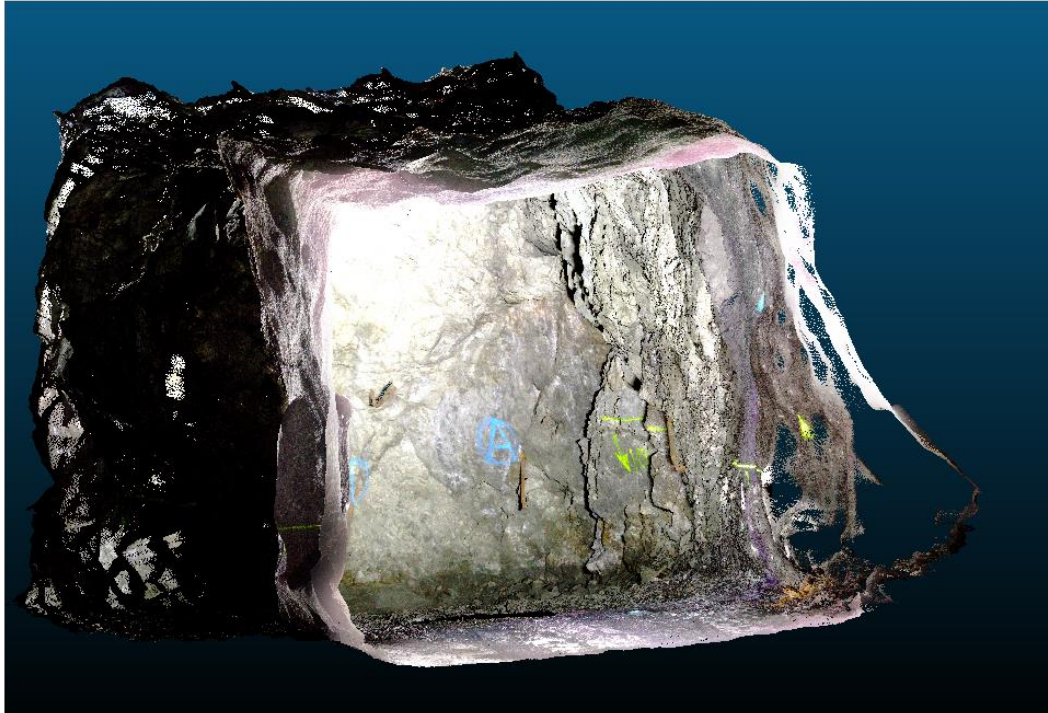


**Figure 19: Clipped section of the relevant portion of the point cloud obtained with TLS in CloudCompare.** This function of the software enabled the user to delete sections of the point cloud that were not considered valuable for the aim of this study, maintaining only the more point-dense part of the cloud where most of the important information was retained.

At this stage, the point cloud could be exported as a .las file format which is compatible with Unity and thus enabling the consequent creation of a VR model with a point cloud. However, in this study this option was not considered since the purchase of a plug in is necessary to import a point cloud to Unity. Considering that the outputs of the 3DScannerApp are meshes and after detailed analysis of CloudCompare's functions, this software was further used to convert this point cloud into a mesh, allowing the comparison of the two scanning methods and of 3D object creation. By constructing faces connecting the points of the cloud, using the function Poisson Surface Reconstruction, 3D objects were created. According to Kazhdan, et al. this method of surface reconstruction allows a great detail by considering all points at once as a spatial Poisson problem<sup>49</sup>. Where the input is the point cloud, and by defining the depth of octrees, the algorithm generates the surface from which the points belong with incremented detail the greater the depth is<sup>49</sup>. However, by increasing the octree depth, the model's running time and memory performance can increase by a factor of four<sup>49</sup>.

In this case study, the octree depth defined was 10 (Figure 20), this allowed for a considerate detail in the mesh without an exorbitant use of memory and time consumption while managing the model. Other depth levels were considered such as 12, however the surface took over an hour to construct and resulted in a file larger than 5GB, leading to a file that was impossible to manage without constant crashing of the computer. Nevertheless, it is important to note that this boundary is strictly imposed by the computational capabilities of the device where the models were being generated, and thus more potent devices may reach a deeper level of detail.

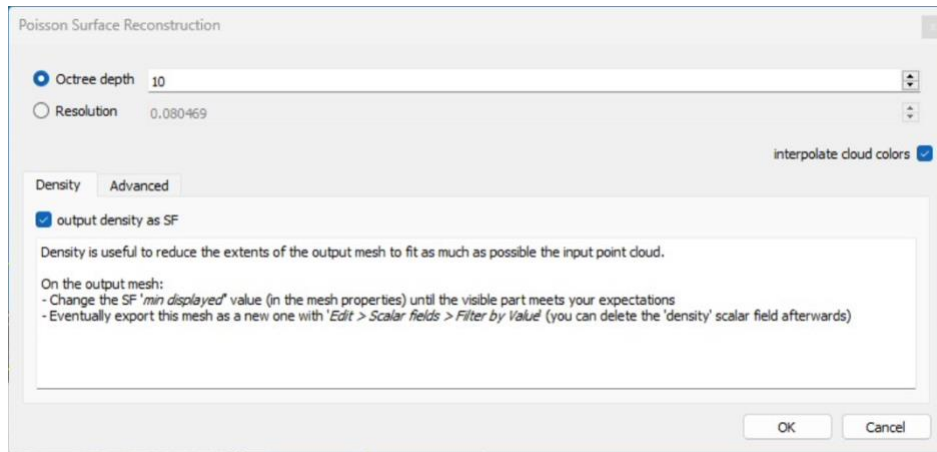


**Figure 20: Configuration of the Poisson Surface Reconstruction parameters in CloudCompare.** The octree depth is positively correlated with the resolution and detail of the surface<sup>49</sup>, whereas the option to have the output density as a Scalar Field (SF) enables the user to identify the areas of the mesh with higher concentration of points and thus higher resolution.

By choosing the option “output density as SF”, the result appeared as a colorful mesh where the density of points, and thus the resolution of the reconstruction, is scaled from lower to higher quality ranging from blue, to green, yellow and red, with the red areas being the ones with greater detail. As shown in Figure 21, the central area of the drift had a higher density of points, whereas the areas with the lowest point density correspond to the edge of the point cloud and the area on the ground where the laser scanner was stationed. Moreover, it is evident that in the roof and walls of the last 2 to 3 meters of the drift, the density of points is also inferior, this can be due to the irregularity of the drift leading to some areas being “shaded” from the scanner.

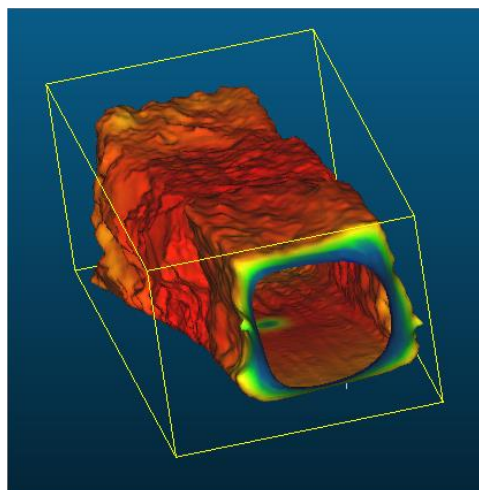


**Figure 21: Generated surface using CloudCompare’s Poisson Surface Reconstruction function.** The color scheme indicates where the areas are with a higher (red, warmer colors) and lower (blue and green, colder colors) density of points.

Afterwards, it was possible to filter the outliers in order to have a mesh containing only the information which is considered viable and that mostly resembles reality. In Figure 22 it is noticeable that by elevating the scalar field minimum values, the mesh deletes the triangles formed with a lower density of points.

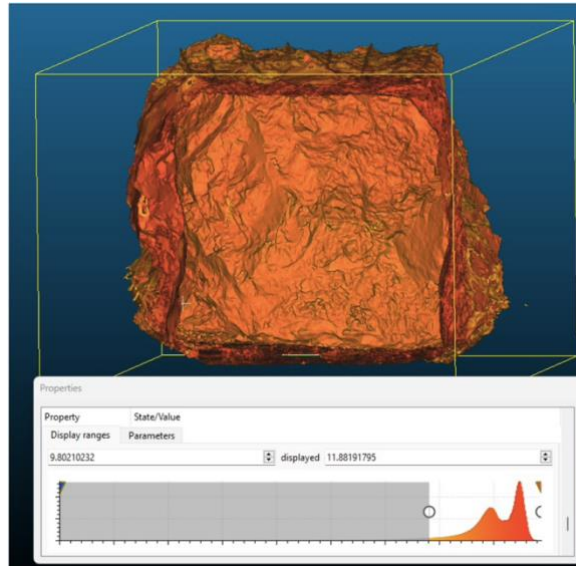


**Figure 22: Final surface after filtering the values with the least information, resulting in a mesh with triangles formed only with a high input of vertices.** This process reduces the size of the mesh, and simultaneously allows for a better representation of the studied object, since the created faces correspond to the faces with a higher confidence level.

By comparing the point cloud originated from the Faro Focus laser scan and the mesh created from it, it is possible to do a qualitative analysis and comparison of both the representation methods. In the Figure 23 it is noted that the details of the irregularities in the face of the drift become more evident when depicted in the mesh, whereas the discontinuities families shown in the sidewalls appear to have identical definition.

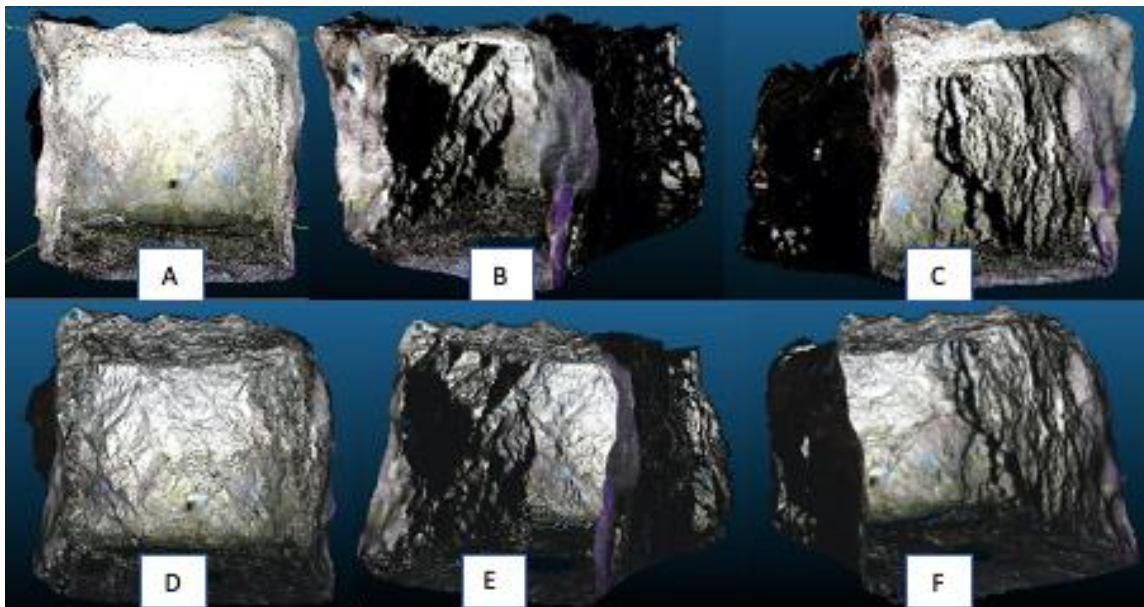


**Figure 23: Comparison between the point cloud obtained through TLS and the mesh generated from it in CloudCompare.** Panels A), B) and C) correspond to the point cloud whereas panels D), E) and F) to the mesh.

The mesh generated with CloudCompare software could then be imported to Unity software. However, considering the file format, it resulted in the VR software not being able to read the texture of the file. Thus, this

mesh was further processed before being brought to unity to develop the VR model. It was necessary to export it as .ply format, then import this mesh to MeshLab (MeshLab 2022.02, 2022) to convert it from .ply to .dae format, allowing for the further importation of the mesh along with its color and texture in Unity. Figure 24 represents the mesh visualization in the MeshLab software.

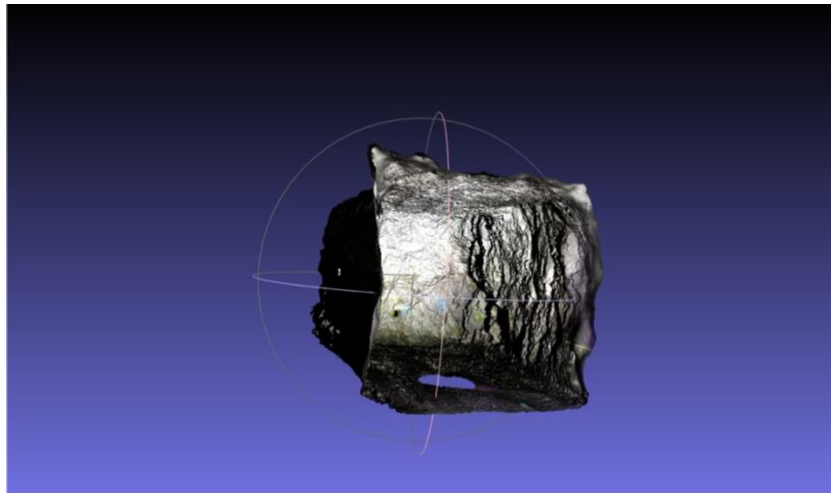


**Figure 24: Visualization in MeshLab of the mesh generated in CloudCompare.** Resulting from the Poisson Surface Reconstruction method applied to the point cloud captured with the Faro Focus S70. As noticeable, the transformation of the mesh from .ply to .dae does not affect in any way the aspect or properties of the mesh.

Afterwards, by installing in Unity the free Unity Package “standard shader with vertex colors”, the .dae file was imported to Unity and the material type changed to *Sprites*, allowing the visualization of the mesh with its texture and color, which were saved into its vertices. Figure 25 shows the final result of the mesh imported into the Unity Scene.

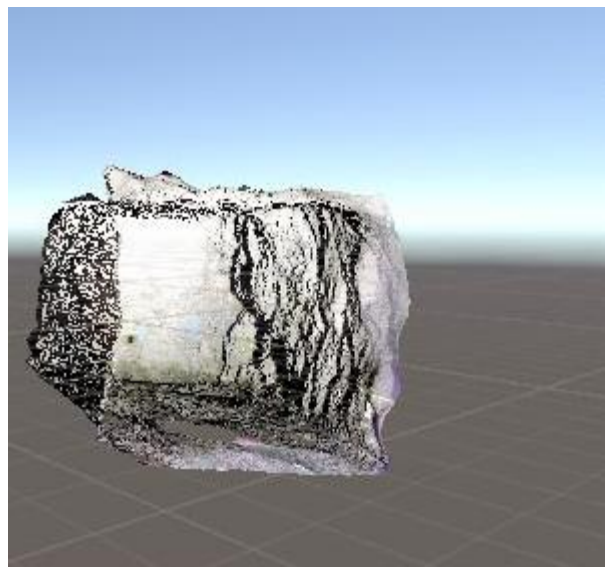


**Figure 25: Preview of the Faro Focus Scan with Unity.** It is possible to visualize that the model was successfully imported with its texture.

At this point the data processing of the point cloud to create a VR model is complete and it is possible to commence the creation of the VR environment with this scan. In order to do so, the same process described for the iPhone scan was followed, consisting of the creation of a floor plane and the installation of the free Unity XR Toolkit plugin to create virtual hands and enabling the camera to be located in the level of the user's eyes through the VR glasses. Allowing the user to freely walk in the model and visualize the points where the glasses are focusing on.

A different approach was considered to develop model 3, since the mesh generated from the point cloud is a very large file, resulting in difficulties in the program processing to capture real-time image during the visualization of the model 2. Thus, an extra step was required to compute a *low-poly* mesh in blender (Blender 3.3, 2022). This low-poly mesh consists in a similar mesh of the one of model 2 but with a fraction of the file size, balancing between the small element count and its visual representation<sup>50</sup>. resulting in an obvious decay of quality of the drift representation, however offering a lighter version of the model, resulting in a better real-time visualization.

### 4.3. Classification of Rock Mass – Q System

As mentioned before, one of the objectives of the study is to infer the capability of assessing the lithology, by geological classification using the iPhone and iPad scans and VR models. To achieve this goal it is necessary to possess *a priori* a sufficient knowledge of the rock formation in this mine.

Rock mass classification systems are frequently used in rock engineering and design<sup>39</sup>. The Q-system, applied to stability of underground openings, is based on assessing six rock mass parameters<sup>40</sup>. The six parameters are: Rock Quality Designation (RQD), joint set number (Jn), joint friction number (Jr), joint infill (Ja), the joint water reduction factor (Jw) and the stress reduction factor (SRF). These six parameters allow to estimate the three factors that most influence the rock mass stability<sup>40</sup>: degree of jointing, joint friction and stress. The formula used to calculate the Q-value is represented in Equation 3.

$$Q = \frac{RQD}{Jn} \times \frac{Jr}{Ja} \times \frac{Jw}{SRF} \quad \text{(Equation 3)}$$

Firstly, the point data generated from the iPhone 13 Pro scan, was introduced into the DSE freeware to compute the principal joint set families, by conducting a semi-automatic analysis based on neighboring points coplanarity test<sup>41</sup>. This allows for the definition of the joint set number (Jn).

Rock Quality Designation (RQD) is the sum of the length (between natural joints) of all core pieces more than 10 cm long (or core diameter x 2) as a percentage of the total core length(Equation 4)<sup>40</sup>. Nonetheless, this measure

is prone to sampling bias due to the preferential orientation of the discontinuities<sup>39</sup>. In order to minimize this disadvantage several approaches can be taken, Gigli et al. proposes a semi-automatic cluster analysis of the point clouds in order to retrieve this geomechanical characteristic<sup>42</sup>. However, in this study a simpler approach was followed and the RQD value was calculated by choosing the direction and zone of the faces of the drift where it had more density of fractures, in order to consider a higher factor of safety. This approach mimics the one used by geotechnical engineers in the Neves-Corvo mine, where the RQD is estimated on-site following the Suorineni described method, by measuring a certain length in a straight line and eliminating the pieces smaller than 10cm<sup>43</sup>.

$$RQD = \frac{\text{Total Core Length} - \Sigma (\text{pieces below 10cm})}{\text{Total Core Length}} \times 100 \quad (\text{Equation 4})$$

When calculating the Joint Friction Number ( $J_r$ ), one must take into account the presence of minerals in the discontinuities walls, and their roughness which can be determined by passing the fingers into the joint walls<sup>40</sup>. However this cannot be possible using a laser scan, and thus the  $J_r$  must be determined considering the large scale roughness by evaluating the joints planarity<sup>40</sup>.

To assess joint friction it is necessary to consider the joint infill ( $J_a$ ) number. This takes into account two factors: thickness and strength. That depend on the mineral infill composition.

The joint water reduction factor ( $J_w$ ) is determined based on inflow and water pressure in the underground opening<sup>40</sup>.

Lastly the Stress Reduction Factor (SRF) needs to be taken into consideration. This parameter describes the relation between stress and rock strength around the underground opening<sup>40</sup>. In the Neves-Corvo mine, the opening of this exploration method and orebody considers a SRF of 2.5.

## 5. Results and Discussion

Considering the conducted study, the results are divided into qualitative analysis of the retrieved images, quantitative analysis of the point clouds captured, comparison of the VR models and rock mass classification. Concerning the qualitative analysis, the considered parameters were the geological contacts, the types of support and unscanned areas (holes). Furthermore, the point clouds are also the object of a quantitative analysis, considering the point quantity, surface density and resolution acquired. Relatively to the VR Models, the results presented consist of a qualitative overview regarding the possibility of its creation and user experience. Lastly, the possibility of classifying geomechanically the rock mass through the iPhone 13 Pro laser scans is demonstrated, using the Q-System and the freeware Discontinuity Set Extractor (DSE). Due to the large size of the point cloud obtained with the Faro laser scanner, it was not possible to conduct this classification with the faro scan. Nevertheless, the retrieval of these geotechnical features in high precision scanners and TLS<sup>51</sup>

are already documented and studied<sup>41</sup>. Thus, only data collection with the iPhone 13 Pro was evaluated for rock mass classification. The simulation of block formation using the software UnWedge was also carried out.

### 5.1. Image Capture Qualitative Comparison

The point clouds and meshes obtain with the Apple devices through the mobile application 3DScannerApp demonstrated a competent level of detail. Both methods showed similar practicability, however scanning with the iPhone proved to be easier due to the simple fact that the device is smaller and lighter and thus more comfortable to carry, it was also noted that the shadow of the iPad appears constantly on the scans, which in some cases may be problematic. Furthermore, the software took less than a minute to process the data, resulting in the models being available to visualize in the Apple Device practically instantly. Figure 26 consists of screenshots taken from the app 3DScannerApp, demonstrating what can be observed in the screen as soon as the scans are completed.

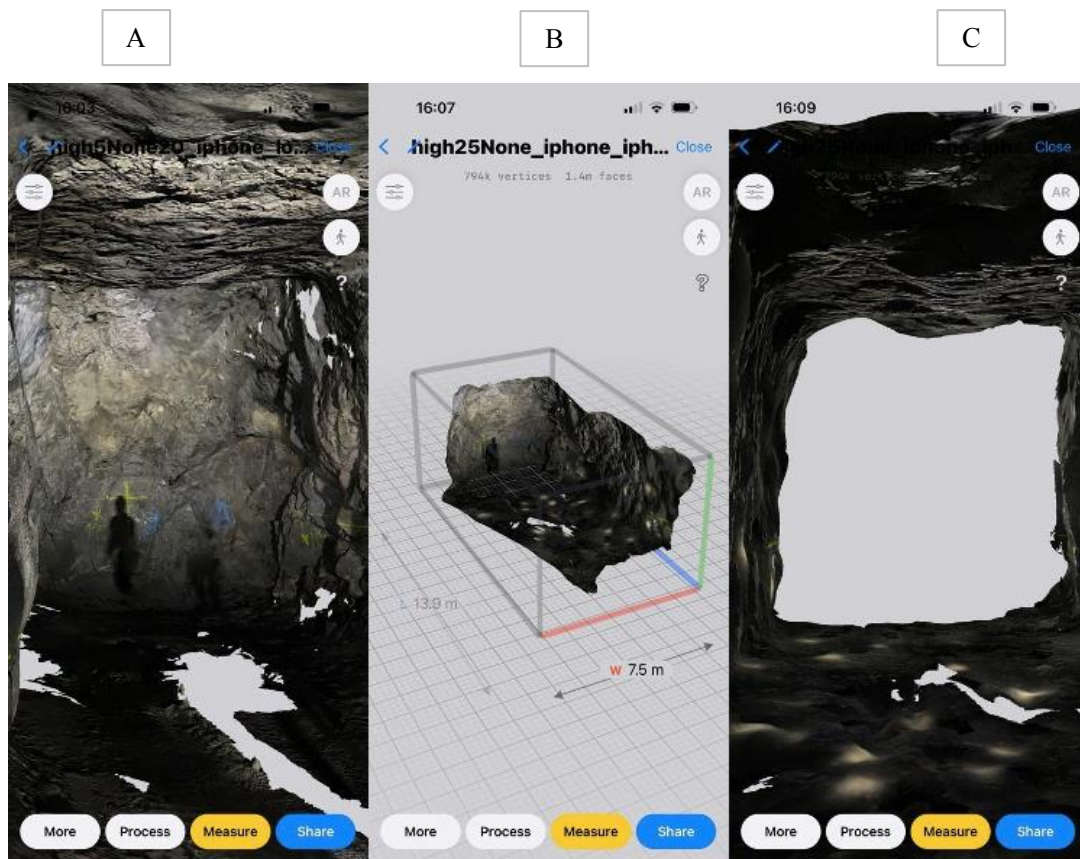


**Figure 26: Screenshots of the iPhone 13 Pro, showing the models generated by the 3DScannerApp.** A) depicts the point of view of the user recording the face of the drift. B) demonstrates a “bird-view” of the entire scanned area, hiding the roof and left sidewall of the gallery. C) depicts the opposite point of view to the drift’s direction, since part of the drift was not scanned, this image shows a blank space, without any data.

By visualizing the models in the app, it is possible to completely rotate and zoom the models into any point of view, allowing the evaluation of the quality of the measurements, the size of the models and the inspection of



the captured images. For instance, in panel A of Figure 26 it is possible to identify the transition between shotcrete and exposed rock and, if the observer has the required geological knowledge, Massive Sulphide and the presence of shales in the left top corner can be identified. Moreover, the scan in the mobile phone provides enough detail to assess the type of support implemented, consisting of expansive bolts in the roof of the gallery and the overall regularity of the drift, as demonstrated in panel C), Figure 26.

With the possibility to assess the different types of support implemented (expansive bolts and shotcrete), it was also possible to review the lithological transition between the massive sulphides and black shales, and since the scan is performed by the user holding the device moving it in order to capture the desired area, it habitates the scanning of surfaces from different angles, that could be “hidden” in a blind spot when conducting a TLS. However, all the scans made with the Apple device were unable to capture the complete surface, always revealing difficulties especially in the ground. Figure 27, obtained from a screen shot from the iPhone that conducted the scans, highlights the different details that were possible to assess through the visualization of the laser scans in the 3DscannerApp environment.



**Figure 27: Highlighted details of the model generated with the iPhone 12 Pro, using the 3DScannerApp.** The green dotted line represents the transition from shotcrete to exposed rock; the red dotted line highlights the transition from exposed massive sulphide to exposed shales; the yellow circles indicate the position of the detected expansive bolts and the areas highlighted in blue are the areas that the device was unable to capture and thus correctly generate a model.

By briefly analyzing the generated model, it is possible to affirm that the recording method positively captured some characteristics already mentioned, which are important when performing a geotechnical evaluation of a site, such as the present lithologies and type of installed support. However, it is clear that this method had trouble recording certain areas of the drift, which can be attributed to the surface of these areas being more irregular or due to the recorder not spending enough time capturing those areas.

Regarding the qualitative results of the point cloud captured with the Faro Focus S70 laser scanner, in Figure 28 it is noticeable that the strong white artificial lighting system of the vehicle lead to the unattainability of the color of the vertices located in the majority of the drift, except the last 14 meters. However, it is evident that the coloration obtained with this scanning method is different to the colors captured with the Apple devices, in reality, the true colors observed *in situ* with the naked eye most resemble the ones obtained with the apple devices. Moreover, due to the reflection of the light in the drifts developing face it is not possible to detect the lithological contact with black shales, detected in the iPhone and iPad scans. Furthermore, the vehicle blocks the path of the light, resulting in large “holes” without vertices beyond the location of the vehicle, nonetheless the part of the drift that was blocked by the vehicle was also not scanned with the apple devices. This scanning method also lead to some point data from certain parts of the drift’s walls being impossible to recover, due to its irregularity and the fact that the laser scanner is static, thus there are areas of the surface which are located in “blind spots” to the scanner, however this can possibly be avoided by proceeding to a MLS method instead of TLS. Nonetheless, the Faro Focus proves to be able to capture the surfaces which are in its line-of-sight with detail, where it is also possible to recognize the rock surface from the shotcrete, the overall irregularity and discontinuities present, the muddy floor and presence of paste fill in the bottom of the drift’s face.

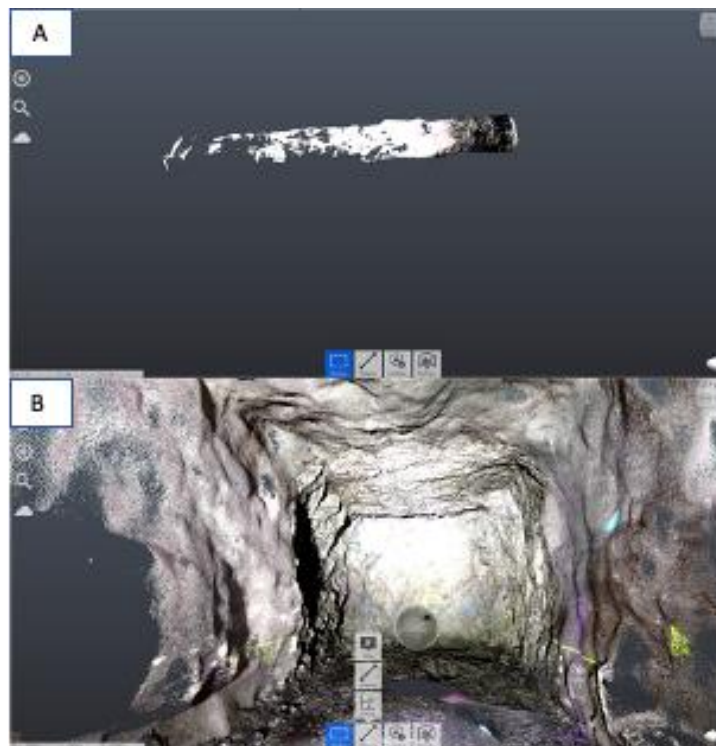
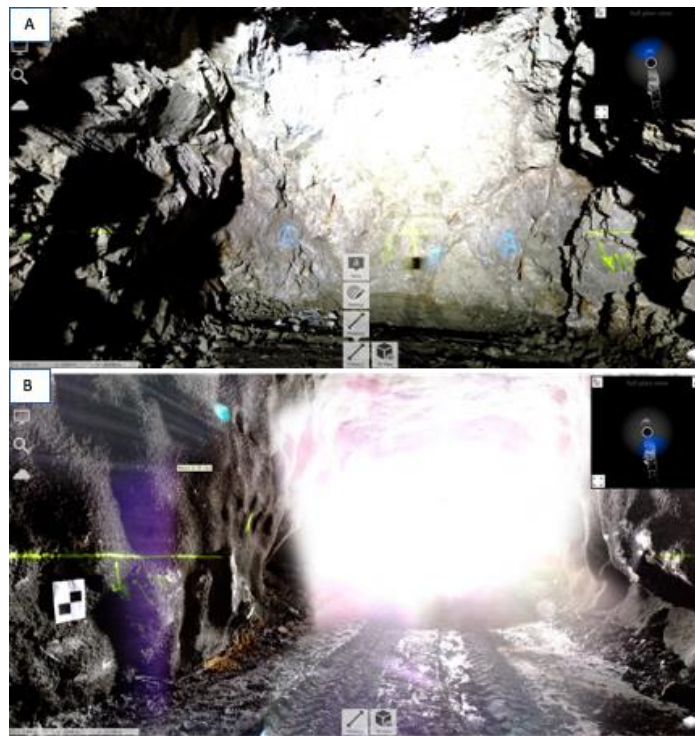


Figure 28: Screenshots of the visualization of the drift’s laser scan in the software ReCap Pro.

In panel A) is possible to see the overall shape of the drift and the fact that the presence of a strong light source blocked the scanner from reading the appropriate colors from most of the point cloud. Furthermore, it is noticeable that the presence of the vehicle hindered the capture of points behind it, leading to a very disperse cloud in the first half of the drift. Panel B) shows the high precision of the scan when it can correctly detect the points, however it is perceivable that due to the static position of the scanner and the irregularity of the walls it could not appropriately read certain points in the sidewalls of the gallery.

By selecting the RealView option it is possible to view the scan from the laser scanner point of view and rotate the camera, as exemplified in the Figures 29. Furthermore, in the same figure, the inclination of the discontinuities of the rockmass, the appearance of paste fill in the bottom of the face coming from the previous levels and also the high reflectance in the face of the drift, due to the strong capture of light coming from the car, are noticeable.



**Figure 29: Screenshot of RealView in ReCap Pro.** Panel A) depicts the point of view from the laser scanner position, facing the face of the drift. Here is possible to assess the inclination of the discontinuities present in the left sidewall and the presence of paste fill in the lower part of the face. Panel B) depicts the point of view from the laser scanner position facing the opposite direction of the face of the drift. It is evident the enormous absorption of white light coming from the vehicle. Nevertheless, it is possible to assess that the drift's floor is muddy and that its sidewalls are to some degree irregular.

In summary, by qualitatively analyzing the two scanning methods, the study demonstrates that the iPhone and iPad revealed to be efficient in the capture of the color, detail of the rock mass and identification of objects present in the scanned surface such as the bolts and shotcrete. Also, by being MLS methods, Apple devices allow for data collection in different angles, avoiding the existence of blind spots. Nevertheless, all the scans conducted with apple devices failed to collect the complete surface, which can be due to the irregularity of the surfaces or

due to human error of failing to point the device to those surfaces for the sufficient amount of time required for data collection. On the other hand, the TLS conducted with the Faro Focus S70 was able to capture any surface as long as it is in its line of sight. Since the scanner is stationary, the recording is not dependent on the movement of the user and is less affected by human error. The static collection of data is also a downside since it leads to the creation of blind spots. Lastly, the scanner properly captured the details of the rock mass irregularity and installed support, despite having issues collecting the true color of the surface due to the impact of the strong artificial light coming from the vehicle. Table 6 summarizes the qualitative comparison of the two methods.

**Table 6: Qualitative Results Summary.** The apple devices were superior in retrieving the color in underground conditions, the overall details such as rock discontinuities and presence of support were captured by both scanning methods, whereas some irregular surfaces were only captured by the Faro Focus S70, however this can be due to the operator not focusing apple devices correctly towards those surfaces. Finally, since the Faro Focus S70 scans were collected as TLS it resulted in the creation of blind spots resulting in failure to capture the complete surfaces.

	Apple Devices (MLS)	Faro Focus S70 (TLS)
<b>Colour</b>	✓	✗
<b>Overall Detail</b>	✓	✓
<b>Capture of Complete Visible Surface</b>	✗	✓
<b>Out of Sight Surfaces</b>	✓	✗

## 5.2. Point Clouds and Meshes Quantitative Comparison

In order to have a practical review of the quantitative results obtained, the scans obtained during the study are also compared to the scan conducted by the Somincor topography team in the Neves-Corvo mine, of the same drift in the same day. This scan was performed with a Leica MS60 laser scanner and was afterwards filtered to reduce its size, allowing its integration in the DeswikCAD software and usage by the mine operations. Figure 30 shows the surface densities obtained with CloudCompare regarding scan 1 conducted with the iPad, scan 2 conducted with the iPhone, the scan obtained with the Faro Focus and the one obtained with Leica MS60, already filtered to be integrated in Deswik. The results show that the Faro Focus scan resulted in the higher surface density, followed by the iPhone, the iPad and lastly the filtered scan used in Deswik.

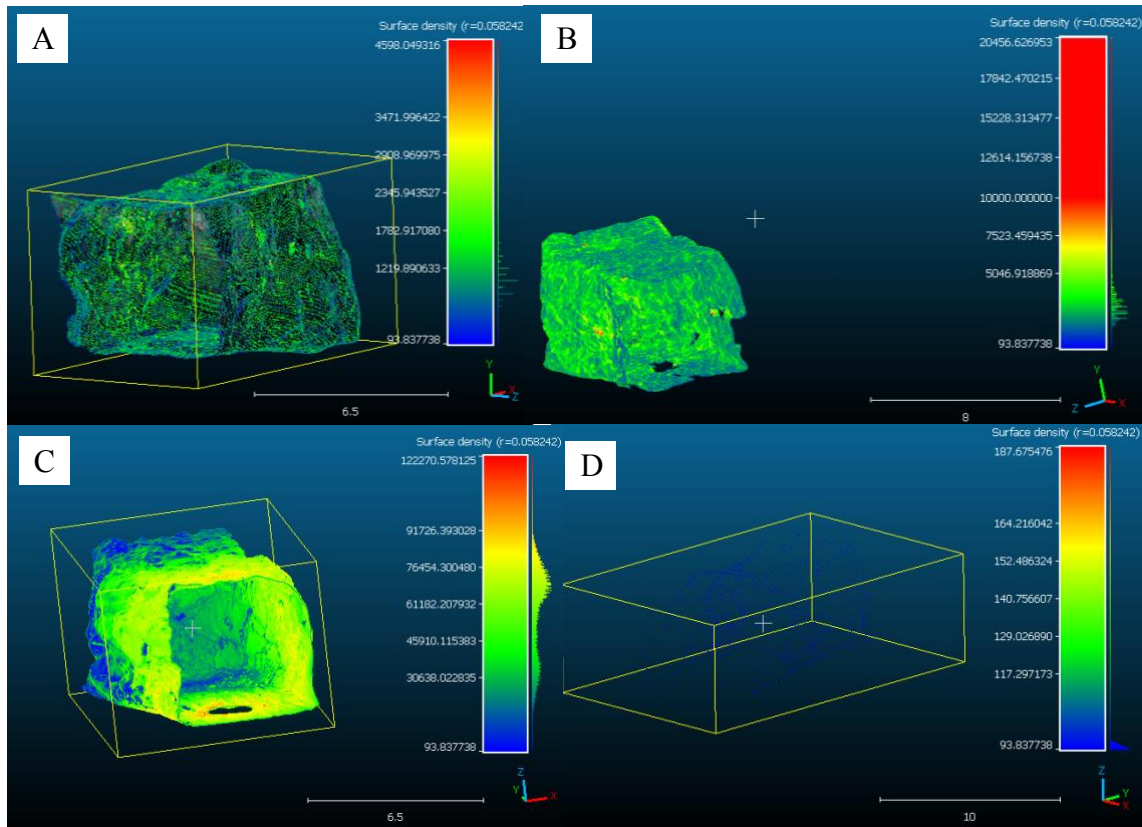


**Figure 30: Surface density representation of different scans.** A) Scan 1; B) Scan 2; C) Scan from model 2; D) Leica MS60 Scan adapted from DeswikCAD. These images show the different surface densities in the scans for the same considered radius of 0.058242m. It is evident that C) captures the highest surface density values with maximum values around 91 000, whereas the iPad scan A) and the iPhone scan B) have maximum surface densities values of approximately 1 800 and 5 040, nevertheless, far superior to the scan used in DeswikCAD by the Mining Operations in Somincor, with maximum density values below 100. The radius  $r$  was generated as an output of the calculation of the surface density of scan 1, and then used as an input for the following surface densities calculations, allowing for a proper comparison metric.

As depicted in Figure 30, the scan captured with the Faro Focus offers the highest surface density values, however its surface density function demonstrates a heterogenic behavior with two relative maximums, resulting in areas of the graphic being depicted with a blueish color (surface density lower) opposed to areas with a green and yellow coloration (higher surface density). The scans obtained with the Apple devices show similar homogenic behaviors, although at different scales. Thus, the representations of surface densities do not reveal areas with substantially different values. The 3D model of the drift used in the Mining Operations offers an inferior result in the metric of surface density. Table 7 describes the characteristics regarding the Leica obtained model.

**Table 7: Characteristics of the Leica BLK generated mesh adapted to DeswikCAD.**

Leica MS60 Generated Mesh adapted to DeswikCAD	
Number of points	1 071
Number of faces	2 138
Average point per face ratio	0.501
Approximated scanned drift length (m)	18.2
Average number of points captured by linear meter	58.8
Scanned Surface Area (m <sup>2</sup> )	438.8
Point Density (point per mm <sup>2</sup> )	1/409 710.6
Resolution (mm)	640.1

The model used in DeswikCAD consists of 1 071 points and 2 138 faces, with a surface area of 438.8 m<sup>2</sup> resulting in a resolution of 640.1mm.

Table 8 presents a summary of the properties of the meshes created by the 3DscannerApp as the output of the drift scanning.

**Table 8: Characteristics of each of the four meshes generated by scans recorded with the 3DscannerApp.** The table displays the number of points and faces per scan, the point to face ratio, the length of the drift that was captured and the points generated by linear meter, the scanned surface area, the density of points and the obtained resolution.

3DscannerApp Generated Mesh Characteristics				
Mesh Scan	1	2	3	4
Number of points	216 886	885 355	393 034	797 737
Number of faces	348 239	1 389 909	606 164	1 360 801
Average point per face ratio	0.623	0.637	0.648	0.586
Approximated scanned drift length (m)	10.95	15.39	12.59	15.36
Average number of points captured by linear meter	19 807	57 528	31 218	51 936
Scanned Surface Area (m <sup>2</sup> )	219.39	288.429	254.258	278.83
Point Density (point per mm <sup>2</sup> )	1/1011	1/325.8	1/646.9	1/351
Resolution (mm)	31.8	18.0	25.4	18.7

Table 8 shows that the scans 2 and 4, the ones conducted with the iPhone, originated meshes with a far superior number of points and consequently faces than the iPad meshes. Even though these scans surveyed a greater area, the quantity of points captured by meter was also substantially greater, also resulting in the generation of a superior number of faces. On the other hand, despite this larger basis of points, the ratio of points per face is

very similar between the four considered meshes, ranging from 0.586 to 0.648 points per face. The resolutions range from 31.8mm to 25.4mm for the iPad scans and from 18.7mm to 18.0mm in the iPhone scans. All finer resolutions than the one used in DeswikCAD.

Lastly, Table 9, summarizes the quantitative results of the mesh generated in CloudCompare, with the scan performed by TLS.

**Table 9: Characterization of the mesh generated in CloudCompare, with the laser scan performed by TLS.** In this table the same characteristics represented in Table 8 are displayed, but regarding the mesh generated in CloudCompare from the Faro Focus laser scan.

CloudCompare Generated Mesh Characteristics	
Number of points	2 364 361
Number of faces	4 135 771
Average point per face ratio	0.572
Approximated scanned drift length	12.19m
Average number of points captured by linear meter	193 959
Scanned Surface Area (m <sup>2</sup> )	293.123
Point Density (point per mm <sup>2</sup> )	1/123.98
Resolution (mm)	11.1

The number of points captured by linear meter is approximately three times superior relatively to the iPhone surveys and more than five times the ones recorded with the iPad. Nevertheless, the ratio between points and faces is the lowest when comparing with the Apple counterparts, with a difference of 22.22%. Considering the resolution, this method presented the thinner resolution of 11.1mm. Table 10 summarizes the quantitative results obtained with the different devices used.

**Table 10: Comparison regarding the number of points, scanned surface area, density of points and resolution obtained with the four different devices utilized.**

	Leica MS60	5 <sup>th</sup> Generation iPad Pro	iPhone 13 Pro	Faro Focus S70
Number of Points	1 071	393 034	885 355	2 364 361
Scanned Surface Area (m <sup>2</sup> )	438.8	254.258	288.429	293.123
Point Density (point per mm <sup>2</sup> )	1/409 710.6	1/646.9	1/325.8	1/123.98
Resolution (mm)	640.1	25.4	18.0	11.1

As shown in table 10, the number of points registered in the mesh captured by the Leica MS60 is the lowest, despite having the highest scanned surface, resulting in the inferior point density and resolution. Whereas the resolution difference between the iPad and iPhone scans was of 7.4 mm, and from the iPhone to Faro 7 mm. Figure 31 represents the difference in resolutions obtained with Faro Focus S70 and iPhone 13 Pro.

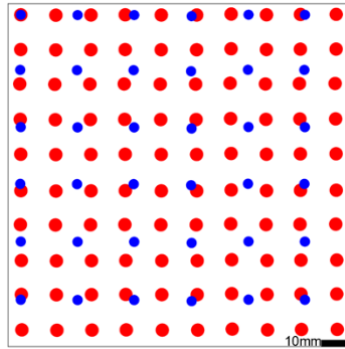


**Figure 31: Scheme representing the different resolutions obtained with the Faro Focus (red) and iPhone 13 Pro (Blue).**

Each dot represents a point captured by the devices. Forming a mesh with a distance between points of 11.1mm in the case of the Faro Focus and 18.0mm for the iPhone, resulting in 100 and 66 points captured on average, by squared meter, respectively.

By analyzing the results obtained in this study regarding the quantitative comparison of the point clouds and meshes, it is possible to affirm that the Faro Focus S70 generated scans resulted in the highest values for points capture, mesh generation, surface density and resolution. Followed by the iPhone and then the iPad generated scans, despite the similar technology implemented between the American company devices. Nevertheless, all scans conducted in this study, revealed superior characteristics regarding the metrics analyzed, when comparing to the 3D model used by the Mining Operations at Neves-Corvo.

### 5.3. VR Models

Both laser scanning methods (TLS with faro focus and MLS with iPhone) were able to produce virtual reality models from the point clouds captured. By performing the laser scans with the Apple devices, the output can be a 3D object such as an .obj or .fbx file. This proves to be an advantage by shortening the pipeline from laser scanner to Virtual Reality model, since the file can be the direct input to Unity, moreover, the texture is saved in a .jpg file as an image, thus can also be directly placed in Unity, making the previous processing of the data before VR model creation obsolete. The perception resulting from the VR models is similar to the one discussed in the point cloud qualitative and quantitative results, where the model created from the iPhone scan presents a truer color despite the lower resolution when comparing to the model from the Faro Focus S70 scan. Figure 32 depicts the user's point of view in model 1's virtual reality environment.





**Figure 32: Model 1 preview in Unity Game, consisting of the laser scan and photogrammetry captured with the iPhone 13 Pro.** While viewing model 1 with the Oculus Quest 2 VR glasses, the user can walk through the drift and turn its head or body in order to look at different points of the gallery.

The faro focus scan requires a more extensive data processing pipeline, due to the incompatibility of file formats, starting as a .fls file as the output of the scanner, being transported to Autodesk ReCap to convert to a .pts point cloud in order to be compatible with CloudCompare, where a mesh is created in the .ply format, which is then converted to a .dae mesh with the texture saved in the vertices in the MeshLab freeware, finally it can be uploaded to Unity to create the VR model. Figure 33 shows the VR Model 2 view from the Unity game.



**Figure 33: Visualization of Model 2 in Unity Scene.** This model consists of the mesh generated from the point cloud captured with the TLS method.

This model, due to the high resolution captured, resulted in a larger file, which can be too heavy to present real time movement when using the Oculus Quest 2, downgrading the user experience. To avoid this, a 3<sup>rd</sup> model was created, also from the Faro Focus S70 scan, where before being uploaded to Unity, the mesh was transformed into a low poly mesh, which consists of diminishing the quantity of vertices and faces at a higher rate than the diminishing of the texture, resulting in a mesh with a lower resolution but as lighter version and able to be more efficiently integrated as a VR model. In Figure 34, the visualization of model 3 in the Unity Scene is displayed.



**Figure 34: Visualization of Model 3 in Unity Scene.** The decrease in image quality when compared to model 2 is evident.

In summary, the quality of the VR models created through Apple devices laser scans are limited by the resolution offered from its scans whereas the VR models created from TLS are limited by the computing power of the VR glasses used and, considering an underground environment, its ability to correctly capture the color. Figure 35 compares the different perceptions in the VR models created, whereas Table 11 describes the file size of the respective models.



**Figure 35: screenshot of the different VR models created using MLS with iPhone 13 Pro and TLS with Faro Focus S70.** Panel A) consists of model 1, created from the iPhone 13 Pro scan; Panel B) is model 2, created from the Faro Focus S70 scan, without diminishing the point density; Panel C) is model 3, obtained by constructing a low-poly mesh in Blender, from the scan conducted with the Faro Focus S70.

**Table 11: File sizes of each virtual reality model.**

Model	Size (KB)
1	99 542
2	562 348
3	7 377

Model 2 presents the mesh with the most points and thus resolution, resulting in the biggest file size at 562 438 KB. This can lead to some problems during the utilization of the VR Model such as absence of fluid movement

or crashing the device. By constructing a low-poly mesh in Blender it was possible to decrease the size of the model to roughly 1.3% at 7 377 KB, despite the loss of resolution, features such as the expansive bolts, shotcrete and discontinuities are still visible. Since the parent mesh of model 3 was the Faro Focus scan, the color depicted is not similar to the one observed *in situ*. Model 1 is 13.5 times bigger than model 3 but still only 17.7% the size of model 2, with a competent representation of coloration despite the weaker resolution.

#### 5.4. Classification of the Rock Mass using the Q System

The scan 2 conducted with the iPhone 13 Pro was evaluated to assess its capability of mass rock classification using the Q System. As mentioned before, this process was not possible to replicate using the faro scan due to its considerably heavier size. Several approaches were carried in order to try to diminish the size of the point cloud, such as splitting the point cloud, eliminating the roof, floor and considering solely the final 10 meters of the sidewalls. However, the point cloud continued to be too heavy to conduct this method with the available computer.

Considering the iPhone 13 Pro scan 2, the software DSE successfully identified six principal joint families, as described in Table 12.

**Table 12: Characterization of the Principal Joint Set Families.** Considering their Dip, Dip Direction and Percentage of Points.

	Dip (°)	Dip Direction (°)	Percentage of Points (%)
<b>Joint Set 1</b>	54.4	256.7	5.43
<b>Joint Set 2</b>	84.7	40.8	7.63
<b>Joint Set 3</b>	64.3	60.5	3.77
<b>Joint Set 4</b>	62.5	78.6	4.10
<b>Joint Set 5</b>	56.6	228.7	4.00
<b>Joint Set 6</b>	76.5	95.1	5.79

Considering that this is a semi-automatic method, it must be reviewed to ensure the correct interpretation of the results. Figure 36 represents the joint set families identified with DSE (Figure 36, panels A to F), the clusters formed with the dip and dip orientation of the drift's faces (Figure 36 panel G), the stereonet resulting from the clustering (Figure 36 panel H) and the point density representation of the stereonet (Figure 36 panel I).

The algorithm identified the biggest cluster in the points of the roof and floor, due to its regularity (Figure 36 panel G). Followed by a cluster formed by most of the points belonging to the sidewalls of the gallery, also represented in the panel G of Figure 36.

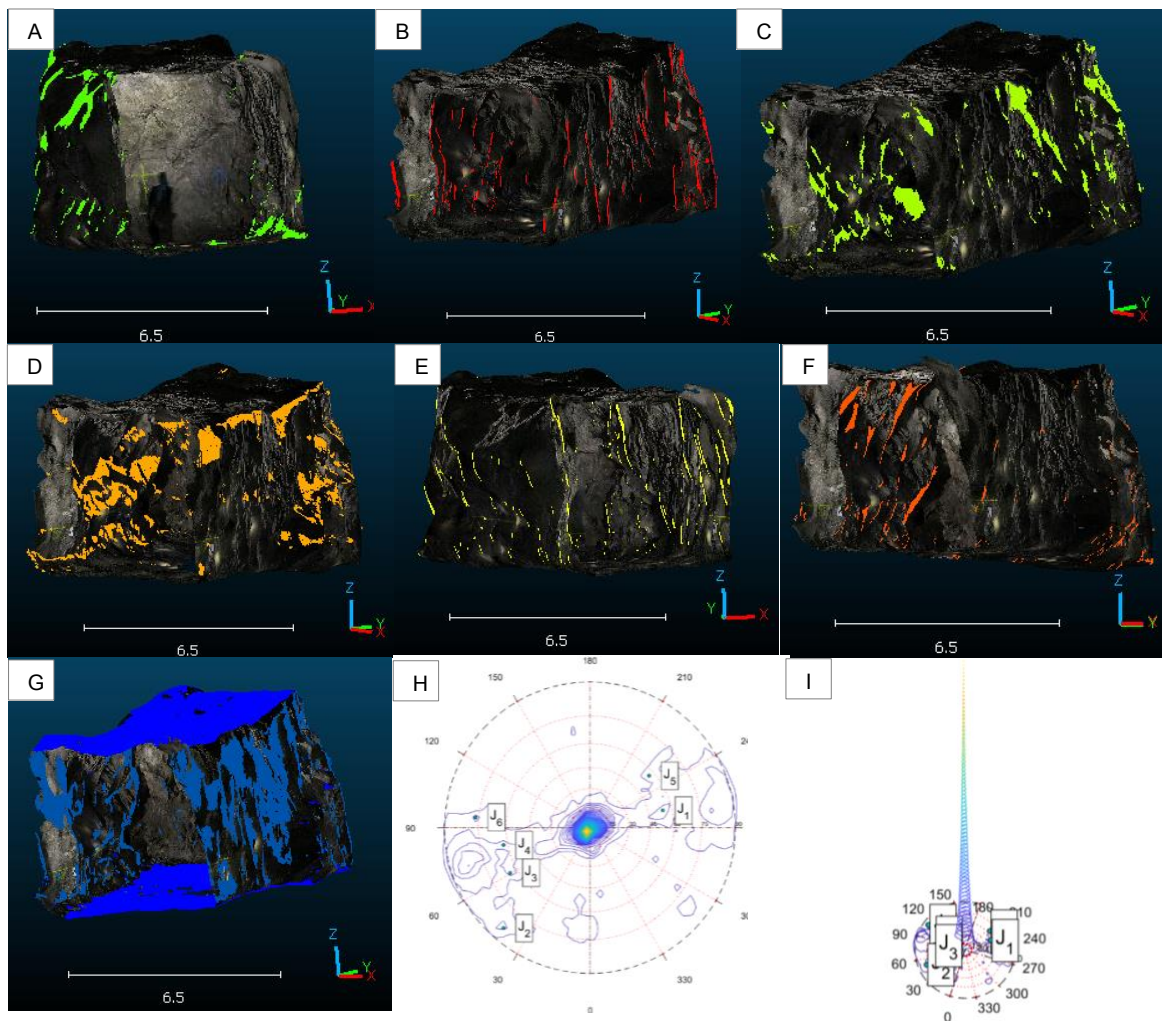
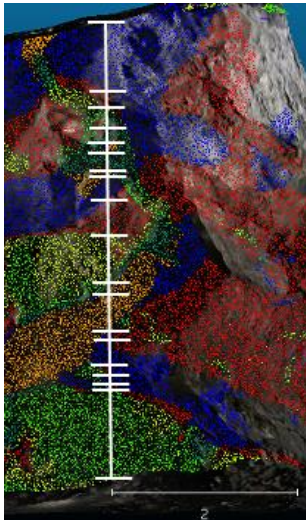


**Figure 36: Clustering results obtained with DSE.** A) Joint set family 1; B) Joint set family 2; C) Joint set family 3; D) Joint set family 4; E) Joint set family 5; F) Joint set family 6; G) Clusters from points located in the roof, floor and sidewalls of the drift; H) Stereonet representation of the generated clusters; I) Density representation of the clusters in the stereonet.

With this software it was possible to correctly identify discontinuity families with different densities, orientations and dips in an underground drift, without the necessity of a high-resolution laser scan. Furthermore, it allowed the visualization of the density of points belonging to each cluster (Figure 36 panel I), it is evident that due to the regularity of the drifts floor and roof, the biggest cluster is formed with points located there, thus resulting in the higher density.

With these results it was possible to define the Joint Set number ( $J_n$ ). Despite the output being of 6 joint set families, it was important when calculating the joint set number, to consider only the joint families that could define a block<sup>40</sup>, in order to avoid reaching a  $J_n$  that was too high and unrealistic. Taking into account that JS3 and JS4, and JS2 and JS5 are characteristically very similar, the first pair being two diagonal families pending to East and the latter two subvertical families and that JS6 has low representativity outside the west wall, the  $J_n$  defined for this excavation should be 12, considering three main joint sets plus random joints<sup>40</sup> assuming JS1 as an isolated joint set, JS2 and JS5 as one joint set, JS3 and JS4 as other joint set, and JS6 representing random joints.

By allowing a highlighted visualization of the discontinuities in the 3D model, this representation could also assist in practical calculations of the RQD, as shown in Figure 37, through Equation 5.



$$RQD = \frac{5.00m - 0.87m}{5.00m} \times 100 \approx 83 \quad \text{(Equation 5)}$$

**Figure 37: Zone of the drift with the highest density of discontinuities.** The vertical line represents the total core length, while the horizontal lines represent the different intervals of continuous rock. From the floor to the roof, the 2<sup>st</sup>, 3<sup>rd</sup>, 4<sup>th</sup>, 6<sup>th</sup>, 8<sup>th</sup>, 12<sup>th</sup>, 14<sup>th</sup> and 17<sup>th</sup> interval were considered to be loose, broken rock. Since, these intervals have a high density of discontinuities passing through them.

By visually analyzing the discontinuities present in the rock mass, they can be classified as rough, from planar to undulating. In order to consider the highest safety approach, the Jr considered was of rough and planar, equivalent to 1.5. Figure 38 depicts the roughness of discontinuities in the eastwall and the table used as a guide, available in the Handbook *Using the Q-System*<sup>40</sup>.

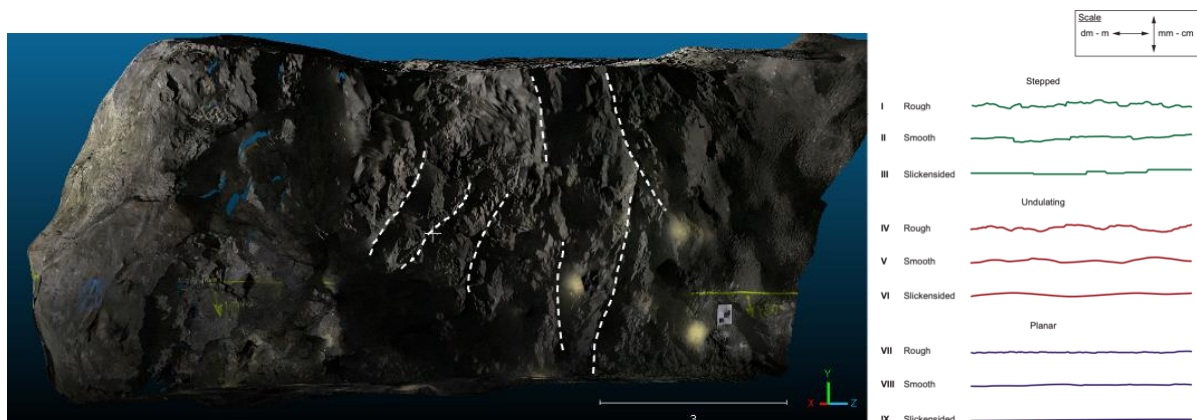


**Figure 38: Discontinuities roughness highlighted in the eastwall of the drift and table<sup>40</sup> with the shape of discontinuities with different levels of roughness.** By comparing the general shape of the discontinuities with the table, and considering the scale, it is evident that the discontinuities present as rough, from planar to undulating.

Considering that it was not possible to view any mineral infilling into the joint walls. The value considered for the parameter of joint alteration, Ja, was of unaltered joint walls, 1.

By viewing the roof of the drift, shown in Figure 39, it is evident that there are no signs of humidity or flow of water present, and thus the  $J_w$  considered is of 1, dry or minor inflow.

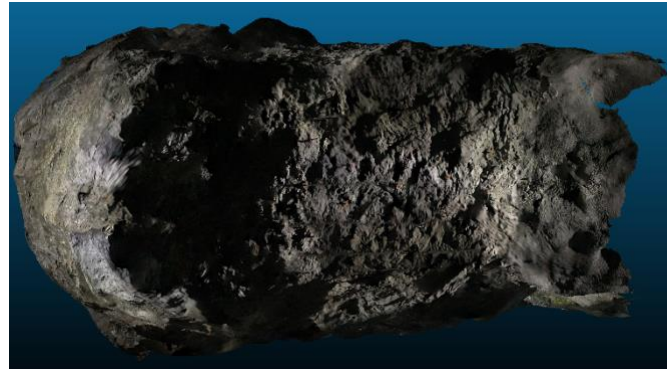


**Figure 39: Display of the roof of the drift, without any evidence of humidity or water flow.**

Lastly the Stress Reduction Factor (SRF) needs to be taken into consideration. This parameter describes the relation between stress and rock strength around the underground opening<sup>40</sup>. In the Neves-Corvo mine, the opening of this exploration method and orebody consider a SRF of 2.5.

After the determination of all needed parameters (Table 13), through the laser scan captured with the iPhone 13 Pro, it was possible to assess the quality of the rock by calculating the Q-value.

**Table 13: Estimated parameters, through the laser scanner captured with the iPhone 13 Pro, used to calculate rock mass quality according to the Q-System.**

Q-System Parameters	
RQD	83
$J_n$	12
$J_r$	1.5
$J_a$	1
$J_w$	1
SRF	2.5
Q	4.2

This evaluation of the rock quality made by assessing the geomechanical characteristics with the scan generated by the iPhone 13 Pro, resulted in classifying the rock as FAIR (Q value between 4 and 10). This value is in accordance with the typical values (FAIR to GOOD) made with conventional methods by geotechnical engineers at the Neves-Corvo mine for the orebody of Neves-South. Furthermore, this data was integrated into the Unwedge software to simulate the block formation in a 5m x 5m drift, as the one presented in the study. The results are shown in Figure 40.

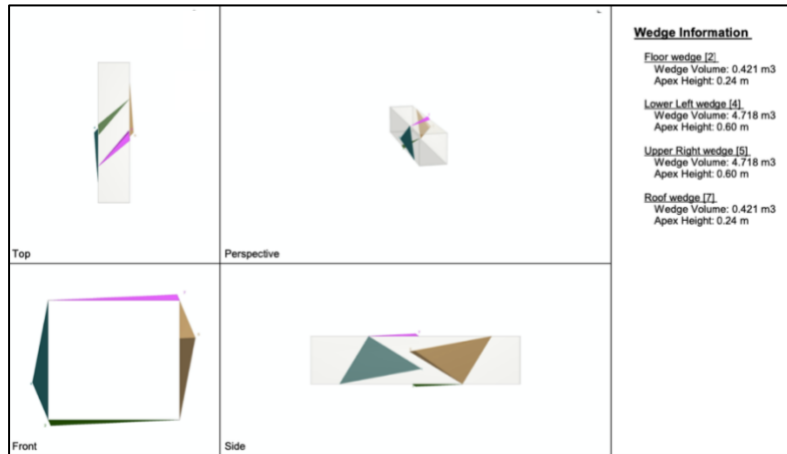


**Figure 40: Unwedge simulation of block formation in a 5m x 5m drift, considering the characteristics retrieved from the iPhone 13 Pro scan.**

The Unwedge simulation obtained with the discontinuity sets extracted from DSE, demonstrated that the sidewalls are at risk of forming bigger blocks than the roof of the gallery. This result is in line with what is expected since the sidewalls of the drift have a higher presence of discontinuities and irregularity, whereas the roof appears to be overall regular. Demonstrating that it is possible to use this type of scans to perform block formation evaluation.

## 6. Conclusions

The iPhone 13 Pro reveals to be a cost-effective and user-friendly alternative to collect 3D data from mine drifts with sufficient detail to retrieve a point cloud dense enough and with sufficient resolution to allow the integration in mining operation systems, with 885 355 points captured in a surface of 288.43 m<sup>2</sup> and a resolution of 18.0 mm, superior to the mesh of the same drift used in Deswik, with 1 071 points in a 438.8 m<sup>2</sup> surface and resolution of 640.1 mm. Considering the 5<sup>th</sup> generation iPad Pro, this device also captured a more detailed point cloud than currently used the mesh, however with lower metrics than the smartphone, furthermore, due to its size and shape it is more difficult to conduct the scanning. The TLS obtained point cloud offered the highest resolution, point density and was able to collect points of all visible surface, nevertheless, due to being stationary, part of the drift becomes inaccessible to the laser scanner, thus leaving the scan with blind spots. Despite the higher resolution of the laser scanner, the imagery obtained with the apple devices revealed a color depiction closer to reality, which is an important feature to consider since valuable information such as rock type and weathering can be obtained through the presented color.

The combination of the point cloud and photography collected with the iPhone 13 Pro proved to be detailed enough to allow rock mass classification in this drift, using the Q-Barton method, and to integrate this data in Unwedge in order to simulate block formation. As mentioned before, the classification of rock masses with 3D point cloud data obtained with professional laser scanners and TLS is already studied and documented, however it could not be investigated in this study, due to the large size of the captured point clouds and the limited computer power of the computer used. This can be interpreted as a limiting factor of conducting rock mass



classification with professional laser scanners since considering the larger files it may require more advanced computing capabilities.

The main limitations identified in the Apple devices' laser scan capabilities consist of the limiting distance of only 5 meters and the overall reduced quality of scanning when compared to professional laser scanners.

Future studies should include coupling the smartphone or iPad to unmanned aerial vehicles (UAV) or quadruped robots, to mitigate the distance restraint. Moreover, to have a better documentation of the limitations and capabilities of these devices, these should be tested in excavations with different geometries and lithologies.

Regarding the creation of VR models, the Apple devices scans require a far less extensive process of data managing, since the output of the scans can be an .obj or .fbx file with the vertices and faces and a .jpg file with the texture, these can be directly imported to Unity to integrate a VR Model. On the contrary, the Faro Focus scans require a more laborious process to get integrated to Unity. Moreover, depending on the VR glasses or computer used, it may be necessary to create a low-poly version of the scan in order to run efficiently as a program. In the VR development field, this study only aimed to investigate the possibility and limitations of integrating an Apple device scan in a VR model of a mine. It is shown that it can be done quite directly, with the main limitations being the quality of the scan and the computing power of the glasses or computer running the simulation. Nevertheless, it is a field with evident potential and allied with game development, the models can be upgraded to allow for rock mass classification, measurement of distances or other features relevant to the mining sector while in the simulated environment.

In summary, the iPhone 13 Pro is capable of being used as a tool to conduct mine drift inspections *ex situ* and a mean to create VR models. And with the constant evolution of these devices and the integration of other science fields such as robotics and game development it can contribute to the digitization and automation of mines.

## Bibliography

1. Berger, S. *Mining history: sub-fields and agendas. Making Sense of Mining History* (2020).
2. Kennedy, B. A. *Surface Mining, Second Edition*. (Society for Mining, Metallurgy, and Exploration, 1990).
3. Meyers, S. & Shanley, E. S. Industrial explosives - a brief history of their development and use. *J. Hazard. Mater.* **23**, 183–201 (1990).
4. Kapagendis, I. K. The Future of Mine Planning Software – New Tools and Innovations. *19th Int. Min. Congr. Fair Turkey IMCET2005* 275–281 (2005).
5. Poniewierski, J. Block model knowledge for mining engineers—an introduction. *Available at: Available at:* 1–33 (2019).
6. Laurence, D. Establishing a sustainable mining operation: an overview. *J. Clean. Prod.* **19**, 278–284 (2011).
7. Faz-Mendoza, A. *et al.* Intelligent processes in the context of Mining 4.0: Trends, research challenges and opportunities. in *2020 International Conference on Decision Aid Sciences and Application (DASA)* 480–484 (2020).
8. Rutkowski, W. & Lipecki, T. Use of the iPhone 13 Pro LiDAR Scanner for Inspection and Measurement in the Mineshaft Sinking Process. *Remote Sens.* **15**, (2023).
9. Wandinger, U. Introduction to Lidar BT - Lidar: Range-Resolved Optical Remote Sensing of the Atmosphere. in (ed. Weitkamp, C.) 1–18 (Springer New York, 2005).
10. Ren, Z., Wang, L. & Bi, L. Robust GICP-based 3D LiDAR SLAM for underground mining environment. *Sensors (Switzerland)* **19**, (2019).
11. Van Der Merwe, J. W. & Andersen, D. C. Applications and benefits of 3D laser scanning for the mining industry. *J. South. African Inst. Min. Metall.* **113**, 213–219 (2013).
12. Rozmus, M. *et al.* Application of 3D scanning, computer simulations and virtual reality in the redesigning process of selected areas of underground transportation routes in coal mining industry. *Energies* **14**, (2021).
13. Filigenzi, M. T., Orr, T. J. & Ruff, T. M. Virtual Reality for Mine Safety Training. *Appl. Occup. Environ. Hyg.* **15**, 465–469 (2000).
14. Bazarnik, M. Slope stability monitoring in open pit mines using 3D terrestrial laser scanning. *E3S Web Conf.* **66**, (2018).
15. Razali, M. I., Idris, A. N., Razali, M. H. & Syafuan, W. M. Quality Assessment of 3D Point Clouds on the Different Surface Materials Generated from iPhone LiDAR Sensor. *Int. J. Geoinformatics* **18**, 51–58 (2022).
16. Paula Martins Falcão Flor Alexandre Bacelar Gonçalves, A. Analysis of a point cloud obtained from merging airborne laser scanning and hand-held mobile laser scanning by iPhone 13Pro. (2022).
17. Luetzenburg, G., Kroon, A. & Bjørk, A. A. Evaluation of the Apple iPhone 12 Pro LiDAR for an Application

- in Geosciences. *Sci. Rep.* **11**, 22221 (2021).
18. Jessy Kartini, G. A., Gumilar, I., Abidin, H. Z., Yondri, L. & Nabil Nugany, M. R. Stonex F6 and iPad Pro M1 2021 for Cave Graffiti Inspection in Barong Cave, West Java, Indonesia. *IOP Conf. Ser. Earth Environ. Sci.* **1127**, 12031 (2023).
  19. Chase, P. P. C., Clarke, K. H., Hawkes, A. J., Jabari, S. & Jakus, J. S. Apple iPhone 13 Pro lidar accuracy assessment for engineering applications. *2022 Digit. Real. Tomorrow* 1–10 (2022).
  20. Torkan, M., Janiszewski, M., Uotinen, L. & Rinne, M. Method to obtain 3D point clouds of tunnels using smartphone LiDAR and comparison to photogrammetry. *IOP Conf. Ser. Earth Environ. Sci.* **1124**, 12016 (2023).
  21. Mastorocco, G., Salvini, R. & Vanneschi, C. Fracture mapping in challenging environment: a 3D virtual reality approach combining terrestrial LiDAR and high definition images. *Bull. Eng. Geol. Environ.* **77**, 691–707 (2018).
  22. Banfi, F., Brumana, R. & Stanga, C. Extended reality and informative models for the architectural heritage: from scan-to-BIM process to virtual and augmented reality. *Virtual Archaeol. Rev.* **10**, 14–30 (2019).
  23. Teppati Losè, L., Spreafico, A., Chiabrande, F. & Giulio Tonolo, F. Apple LiDAR Sensor for 3D Surveying: Tests and Results in the Cultural Heritage Domain. *Remote Sens.* **14**, 0–34 (2022).
  24. Peek, A., Martin, M. & Kolston, S. The Virtual Reality of GIScience. *UC St. Barbar. Cent. Spat. Stud.* **6**, 588–589 (2021).
  25. Martín-Romero, J. L. *et al.* VIRTUAL REALITY IMMERSIVE OF GEOMATIC TECHNIQUES LEARNING. in 7177–7181 (2018).
  26. Dima, E. & Sjöström, M. Camera and Lidar-Based View Generation for Augmented Remote Operation in Mining Applications. *IEEE Access* **9**, 82199–82212 (2021).
  27. Krok, G., Kraszewski, B. & Stereńczak, K. Application of terrestrial laser scanning in forest inventory – an overview of selected issues. *For. Res. Pap.* **81**, 175–194 (2020).
  28. Faro Focus Laser Scanners. (2023).
  29. g2metric. (2023).
  30. Cariou, E., Baltzer, A., Leparoux, D. & Lacombe, V. Collaborative 3d monitoring for coastal survey: Conclusive tests and first feedbacks using the selphcoast workflow. *Geosci.* **11**, 1–16 (2021).
  31. Pfeifer, N. & Briese, C. Laser scanning – principles and applications. (2007)
  32. Zogg, H. & Maar, H. Leica Nova MS60 White paper Leica Nova MS60 – One instrument for all measuring tasks. (2020).
  33. Torino, P. D. I. & Martino, A. Apple 's iPad Pro sensors for Cultural Heritage Documentation. (2022).
  34. Apple. [Internet]. Apple. November 2023. Available from: <https://www.apple.com/>
  35. Mikita, T., Krausková, D., Hrůza, P., Cibulka, M. & Patočka, Z. Forest Road Wearing Course Damage Assessment Possibilities with Different Types of Laser Scanning Methods including New iPhone LiDAR Scanning Apps. *Forests* vol. 13 (2022).
  36. Berdan, R. Digital photography basics for beginners. 1–12.

37. Fryskowska, A. & Wroblewski, P. Mobile Laser Scanning accuracy assessment for the purpose of base-map updating. *Geod. Cartogr.* **Vol. 67, n.**, 35–55 (2018).
38. Vlachos, M., Berger, L., Mathelier, R., Agrafiotis, P. & Skarlatos, D. SOFTWARE COMPARISON FOR UNDERWATER ARCHAEOLOGICAL PHOTOGRAMMETRIC APPLICATIONS. *Int. Arch. Photogramm. Remote Sens. Spat. Inf. Sci.* **XLII-2/W15**, 1195–1201 (2019).
39. Palmstrom, A. & Broch, E. Use and misuse of rock mass classification systems with particular reference to the Q-system. *Tunn. Undergr. Sp. Technol.* **21**, 575–593 (2006).
40. Norwegian Geotechnical Institute. Using the Q-system. *Nor. Geotech. Inst.* 57 (2015).
41. Riquelme, A. J., Abellán, A., Tomás, R. & Jaboyedoff, M. A new approach for semi-automatic rock mass joints recognition from 3D point clouds. *Comput. Geosci.* **68**, 38–52 (2014).
42. Gigli, G. & Casagli, N. Semi-automatic extraction of rock mass structural data from high resolution LIDAR point clouds. *Int. J. Rock Mech. Min. Sci.* **48**, 187–198 (2011).
43. Suorineni, F. T., Kaiser, P. K. & Henning, J. G. Safe rapid drifting – Support selection. *Tunn. Undergr. Sp. Technol.* **23**, 682–699 (2008).
44. Costa, P., Moura, A. & Pacheco, N. Geologia Mineira em Neves-Corvo Acompanhamento de trabalhos de fundo de mina e de prospeção mineira. (2017).
45. Lundin Mining Corporation [Internet]. December 2023. Available from: <https://lundinmining.com/>
46. Carvalho, P. & Ferreira, A. Geologia De Neves-Corvo : Estado Actual Do Conhecimento. *Simpósio Sulfuretos Polimetálicos da Faixa Piritosa Ibérico* 30 (1993).
47. 3D Scanner App. [Internet]. November 2023. Available from: <https://3dscannerapp.com/>
48. How to Make a VR Game in Unity - PART 1 [Internet]. [www.youtube.com](http://www.youtube.com). [cited 2024 Apr 20]. Available from: <https://www.youtube.com/watch?v=HhtTtvBF5bl&list=PLpEoiloH-4eP-OKItF8XNJ8y8e1asOJud>.
49. Kazhdan, M. & Hoppe, H. Distributed Poisson Surface Reconstruction. *Comput. Graph. Forum* **42**, (2023).
50. Gao, X., Wu, K. & Pan, Z. Low-poly Mesh Generation for Building Models. in *ACM SIGGRAPH 2022 Conference Proceedings* (Association for Computing Machinery, 2022). doi:10.1145/3528233.3530716.
51. Riquelme, A., Cano, M., Tomás, R. & Abellán, A. Identification of Rock Slope Discontinuity Sets from Laser Scanner and Photogrammetric Point Clouds: A Comparative Analysis. *Procedia Eng.* **191**, 838–845 (2017).